

NAVAL POSTGRADUATE SCHOOL MONTEREY, CALIFORNIA



THESIS

**AN INVESTIGATION OF THE EFFECTS OF
SECONDARY PROCESSING ON THE
FRACTURE PROPERTIES OF A SiCp-
6XXX Al COMPOSITE**

by

Frank N. Quiles

June, 1996

Thesis Advisor:

Indranath Dutta

Approved for public release; distribution is unlimited.

Thesis
Q615

DUDLEY KNOX LIBRARY
NAVAL POSTGRADUATE SCHOOL
MONTEREY CA 93943-5101

REPORT DOCUMENTATION PAGE			Form Approved OMB No. 0704-0188	
Public reporting burden for this collection of information is estimated to average 1 hour per response, including the time for reviewing instruction, searching existing data sources, gathering and maintaining the data needed, and completing and reviewing the collection of information. Send comments regarding this burden estimate or any other aspect of this collection of information, including suggestions for reducing this burden, to Washington Headquarters Services, Directorate for Information Operations and Reports, 1215 Jefferson Davis Highway, Suite 1204, Arlington, VA 22202-4302, and to the Office of Management and Budget, Paperwork Reduction Project (0704-0188) Washington DC 20503.				
1. AGENCY USE ONLY (Leave blank)		2. REPORT DATE June, 1996		3. REPORT TYPE AND DATES COVERED Master's Thesis
4. TITLE AND SUBTITLE An Investigation of the Effects of Secondary Processing on the Fracture Properties of a SiCp-6XXX Al Composite			5. FUNDING NUMBERS	
6. AUTHOR(S) Frank N. Quiles				
7. PERFORMING ORGANIZATION NAME(S) AND ADDRESS(ES) Naval Postgraduate School Monterey CA 93943-5000			8. PERFORMING ORGANIZATION REPORT NUMBER	
9. SPONSORING/MONITORING AGENCY NAME(S) AND ADDRESS(ES)			10. SPONSORING/MONITORING AGENCY REPORT NUMBER	
11. SUPPLEMENTARY NOTES The views expressed in this thesis are those of the author and do not reflect the official policy or position of the Department of Defense or the U.S. Government.				
12a. DISTRIBUTION/AVAILABILITY STATEMENT Approved for public release; distribution is unlimited.			12b. DISTRIBUTION CODE	
13. ABSTRACT (maximum 200 words) Discontinuous reinforced aluminum (DRA) composites are attractive as structural materials because of their desirable stiffness and strength to weight ratios and relative ease of manufacture. However, they typically display low tensile ductility and fracture toughness. In this work, the impact of post-fabrication deformation processing and heat treatment on the fracture properties of a 17.5 vol. % SiCp reinforced Al 6092 matrix composite is investigated. Process temperature, total strain and strain rate during extrusion were varied in order to explore the feasibility of obtaining Particle Stimulated Nucleation (PSN) of recrystallization during processing, with the goal of refining the matrix grain size. Additionally, various combinations of solution and aging treatments were investigated with the aim of obtaining a number of stable matrix microstructural conditions with varying levels of composite strength and fracture toughness. A preliminary investigation of fracture mechanisms and their dependence on the matrix aging state has also been carried out using optical and scanning electron microscopy (SEM) and differential scanning calorimetry (DSC), and is reported here.				
14. SUBJECT TERMS DRA, TMP, PSN, JIc, KIc			15. NUMBER OF PAGES 96	
			16. PRICE CODE	
17. SECURITY CLASSIFICATION OF REPORT Unclassified	18. SECURITY CLASSIFICATION OF THIS PAGE Unclassified	19. SECURITY CLASSIFICATION OF ABSTRACT Unclassified	20. LIMITATION OF ABSTRACT UL	

Approved for public release; distribution is unlimited.

**AN INVESTIGATION OF THE EFFECTS OF SECONDARY
PROCESSING ON THE FRACTURE PROPERTIES
OF A SiCp-6XXX Al COMPOSITE**

Frank N. Quiles
Lieutenant , United States Navy
B.S., Marquette University, 1988

Submitted in partial fulfillment
of the requirements for the degree of

MASTER OF SCIENCE IN MECHANICAL ENGINEERING

from the

**NAVAL POSTGRADUATE SCHOOL
JUNE, 1996**

ABSTRACT

Discontinuous reinforced aluminum (DRA) composites are attractive as structural materials because of their desirable stiffness and strength to weight ratios and relative ease of manufacture. However, they typically display low tensile ductility and fracture toughness. In this work, the impact of post-fabrication deformation processing and heat treatment on the fracture properties of a 17.5 vol. % SiCp reinforced Al 6092 matrix composite is investigated. Process temperature, total strain and strain rate during extrusion were varied in order to explore the feasibility of obtaining of Particle Stimulated Nucleation (PSN) of recrystallization during processing, with the goal of refining the matrix grain size. Additionally, various combinations of solution and aging treatments were investigated with the aim of obtaining a number of stable matrix microstructural conditions with varying levels of composite strength and fracture toughness. A preliminary investigation of fracture mechanisms and their dependence on the matrix aging state has also been carried out using optical and scanning electron microscopy (SEM) and differential scanning calorimetry (DSC), and is reported here.

TABLE OF CONTENTS

I. INTRODUCTION	1
II. BACKGROUND	3
A. GRAIN REFINEMENT BY PARTICLE STIMULATED NUCLEATION (PSN) OF RECRYSTALLIZATION	3
B. AGING IN Al-Mg-Si ALLOYS AND Al-Mg-Si MATRIX DRA	13
C. MECHANISMS OF DEFORMATION AND DAMAGE IN DRA	15
D. INTRINSIC PARAMETERS AFFECTING FRACTURE RESPONSE	17
1. The Reinforcement	17
2. The Matrix	21
3. The Reinforcement-Matrix Interface	21
III. EXPERIMENTAL PROCEDURE	27
A. MATERIAL	27
B. PROCESSING	27
C. MECHANICAL TESTING/SAMPLE PREPARATION	29
D. POLISHING SCHEDULE	33
E. TESTING	33
F. INTERPRETATION AND ANALYSIS OF RESULTS	33
G. DETERMINATION OF J_{Ic} FROM LOAD-DISPLACEMENT RECORD IN THE ABSENCE OF UNLOADING COMPLIANCES	36
IV. RESULTS AND DISCUSSION	43
A. PRIOR MICROSTRUCTURAL FINDINGS	43
B. MICROSTRUCTURAL FINDINGS RESULTING FROM THE NOTCHED TENSILE SAMPLES	43
C. MECHANICAL PROPERTIES	49
D. MICROSTRUCTURAL EVOLUTION DURING PROCESSING AND IT'S IMPACT ON PROPERTIES	62
V. SUMMARY	75
VI. CONCLUSIONS	77
LIST OF REFERENCES	79
INITIAL DISTRIBUTION LIST	83

ACKNOWLEDGEMENTS

Accomplishments are rarely completed without the assistance of colleagues, friends and family members. I would like to thank Prof. Indranath Dutta for his assistance and guidance throughout the thesis work, thus enabling the learning experience to continue. Numerous conversations and valuable time was offered by Prof. T.R. McNelley and Prof J. Wells which fine tuned many misguided thoughts, and these efforts must not go unrecognized. Rich Hashimoto was an invaluable sounding board for ideas and a reliable research assistant. Furthermore, acknowledgements are forwarded to Mr. Mark van den Bergh of DWA Composites for supplying the material, and the staff and faculty at Wright Laboratories at WPAFB, OH for assistance in processing the DRA. Finally, I would like to recognize the never-ending support which my wife Christine and daughter Katherine have consistently provided during this experimentation. Their sensitive insight and eternal patience have undeniably inspired the completion of this research.

I. INTRODUCTION

Energy efficient automobiles and high performance aircraft require strong, stiff and lightweight materials which have prolonged lifespans. The ability to create materials which are capable of achieving the Herculean standards imposed by technological innovations has become a challenge for material scientists. Developing reliable composites which meet or exceed these demands pose the most promising solutions.

Materials presently in service for the aerospace and automotive industry, such as monolithic aluminum alloys, possess inadequate stiffness-to-weight and strength-to-weight ratios and must be improved, especially if the performance of these systems is to continue to surpass their present capabilities. One approach to achieve this end is to reinforce conventional metallic materials with ceramics, thus enhancing the strength and stiffness substantially with little or no penalty in weight.

Composite material reinforcements may be either continuous in the form of a fiber or discontinuous in the form of whiskers or particles. While continuous fibers offer the most stiffness in their longitudinal direction, their properties are highly anisotropic, limiting their applications to situations where this is not a handicap. Particulate reinforced composites, on the other hand, are fairly isotropic, and may be substituted easily for conventional materials used at present. Moreover, the production of discontinuously reinforced composite is cheaper and easier than their continuously reinforced counterparts, making them attractive for a number of military and commercial applications.

One such application, which has been successfully utilized by the U.S. Air Force under the Title III program is the use of discontinuously reinforced aluminum (DRA) composites to replace short lived aluminum aircraft parts, resulting in huge increases in component life cycles. Another potential application of DRA, of interest to the U.S. Army, is as a material for ground vehicles. Both these applications, however, necessitate levels of damage tolerance and fracture toughness of these composites that are not readily achievable. Therefore, despite its potential, DRA has not been widely accepted as a reliable structural material in military and commercial

applications. In order to justify higher manufacturing costs accompanying the improvements in stiffness to-weight and strength-to-weight ratios, the fracture toughness obstacle must be overcome before DRA receives widespread acceptance.

Accordingly, the goal of this work is to investigate various post-fabrication extrusion processes and annealing/aging treatments as avenues to produce DRA with a number of stable microstructural conditions with different combinations of strength and fracture toughness.

II. BACKGROUND

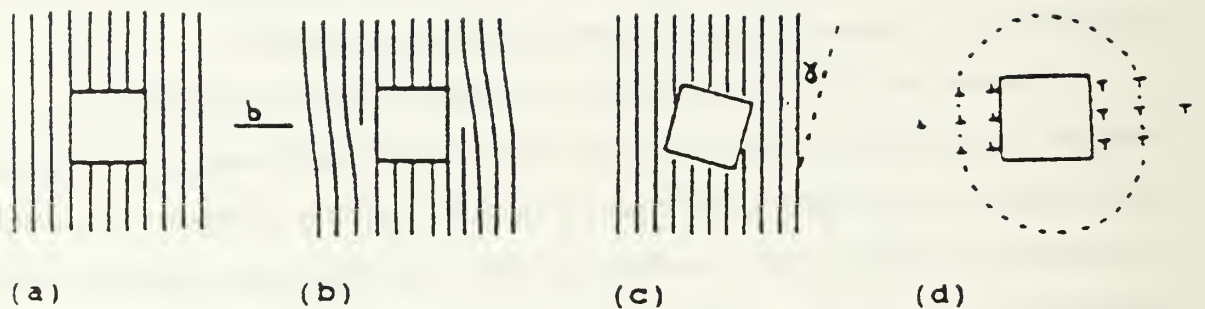
A. GRAIN REFINEMENT BY PARTICLE STIMULATED NUCLEATION (PSN) OF RECRYSTALLIZATION

DRA is usually brittle when in the as-fabricated state. However, post fabrication deformation processing (e.g. hot extrusion) has been previously found to improve the mechanical properties of DRA substantially, in some cases yielding tensile properties comparable to those of unreinforced aluminum alloys [Ref. 1]. This improvement was associated with (1) dispersion of the clustered Al_2O_3 reinforcement particles and (2) matrix microstructural refinement during thermomechanical processing (TMP).

Post-fabrication TMP may induce Particle Stimulated Nucleation (PSN) of recrystallization of matrix grains [Ref. 2-3]. This mechanism has the potential for producing a much finer matrix grain size relative to conventional recrystallization because of the proliferation of nucleation sites in particulate containing materials. The underlying mechanism of PSN of recrystallization may be summarized as follows.

In order for PSN to occur, two conditions must be met: (1) a deformation zone must be created at the particle, and (2) the matrix must have enough stored energy for a nucleus to grow away from the particle. During deformation processing, matrix dislocations are generated at the reinforcement particle perimeter due to the mismatch of large undeformable particles and a deformable matrix. Large strains imposed upon the composite generate dislocation configurations which depend primarily upon the size of the particles and their shape. A plastic relaxation occurs surrounding the particles which results in a rotation of the associated volume with respect to the surrounding matrix. A schematic representation of this rotated deformation zone is shown in Figure 1 [Ref. 3]. During annealing (either during or following deformation), these deformation zones with large matrix lattice rotations (i.e. large stored strain energy) act as preferred sites for nucleation of recrystallized grains, thus resulting in PSN.

Humphreys [Ref. 2] investigated the nucleation of recrystallization at large second phase particles in deformed Al alloy single crystals and found that both nucleation and growth rates



a undeformed: *b* deformed and unrelaxed: *c* relaxation by rotation; *d* formation of impenetrable rotated zone close to particulate at larger strains

2 Schematic diagram of plastic relaxation at large particle

Figure 1: Schematic diagram of plastic relaxation at large particle. From Reference [3].

increase with increasing particle size. Additionally, it has been found that the final grain size due to PSN may be determined by both the particle size and the interparticle spacing. Further, larger reinforcement particles were found to be more efficient at stimulating PSN, which seemed to occur only above a critical particle size. However, this critical particle size was observed to decrease with increasing process strain and increasing strain rate during deformation, both factors helping to result in larger matrix lattice rotations next to the particles (i.e., larger stored strain energies).

Humphreys [Ref. 3] showed that the resulting grain size, D , corresponding to one grain nucleated per reinforcement particle, is expressed by the relationship:

$$D = d / F_v^{1/3} \quad (1)$$

where F_v = volume fraction of reinforcement particles, d = particle size

Figure 2 [Ref. 3] shows the grain size as predicted by Equation (1). Further investigation by Humphreys revealed pinning of the grains by oxide particles and a decrease in driving force (dislocations) as recrystallization progresses. Therefore, a better empirical relationship was developed where [Ref. 3]:

$$D = kd^{1/2} / F_v \quad (2)$$

where k is a proportionality constant.

Because of the requirement of storing a large amount of strain energy (lattice rotation) in the matrix next to the reinforcement particles, the temperature and strain rate during deformation processing are critical to the occurrence of PSN during subsequent annealing. Figure 3 [Ref. 3] shows the temperatures below which adequate stresses can accumulate in the matrix during deformation for various combinations of particle size and strain rate during TMP.

Particulate volume fraction also plays a role in the nucleation of recrystallized grains. This is illustrated by Figure 4 [Ref. 3], which shows that whereas large particle sizes and reinforcement volume fractions are more likely to induce PSN of recrystallization, at small

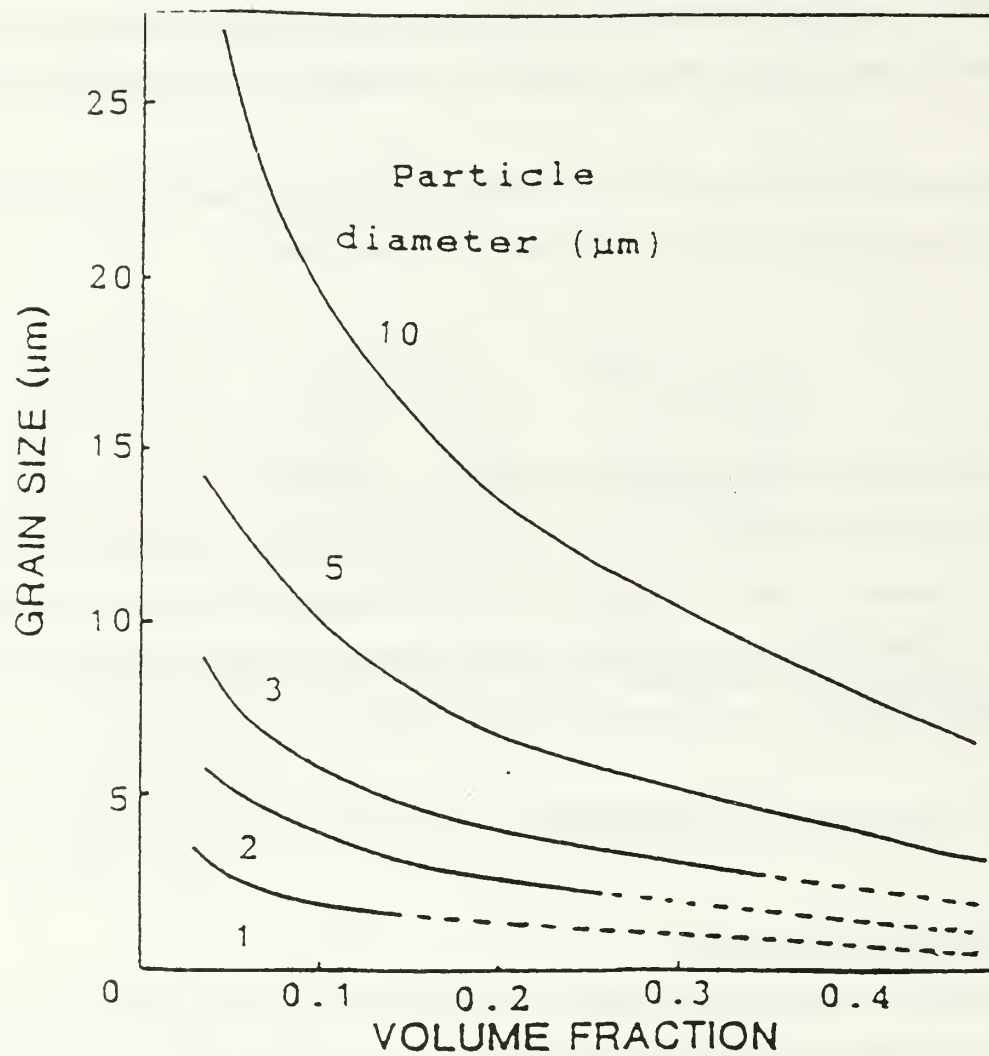


Figure 2: Grain size predicted on basis of particle stimulated nucleation of recrystallization.
From Reference [3]

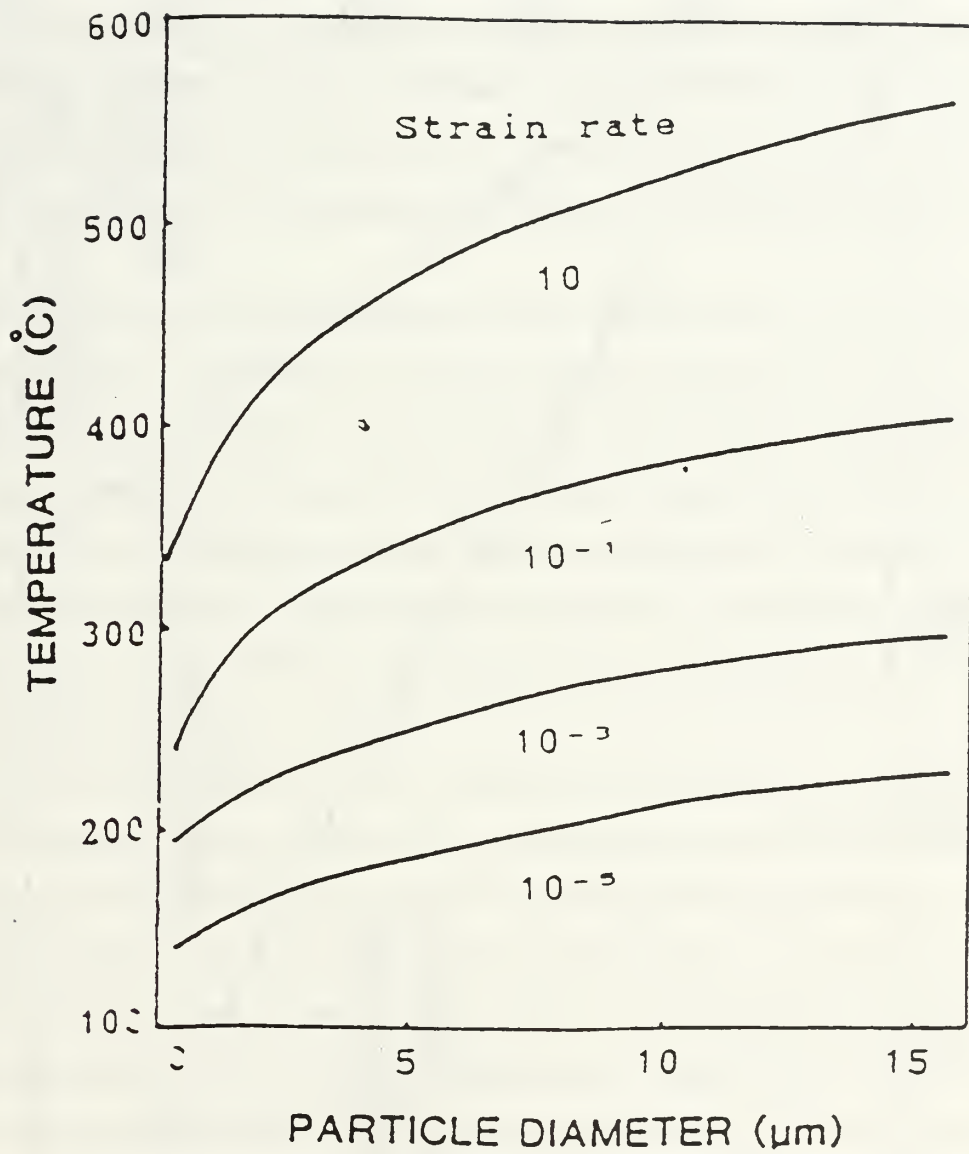


Figure 3: Critical temperature below which stresses will accumulate at particles. From Reference [3].

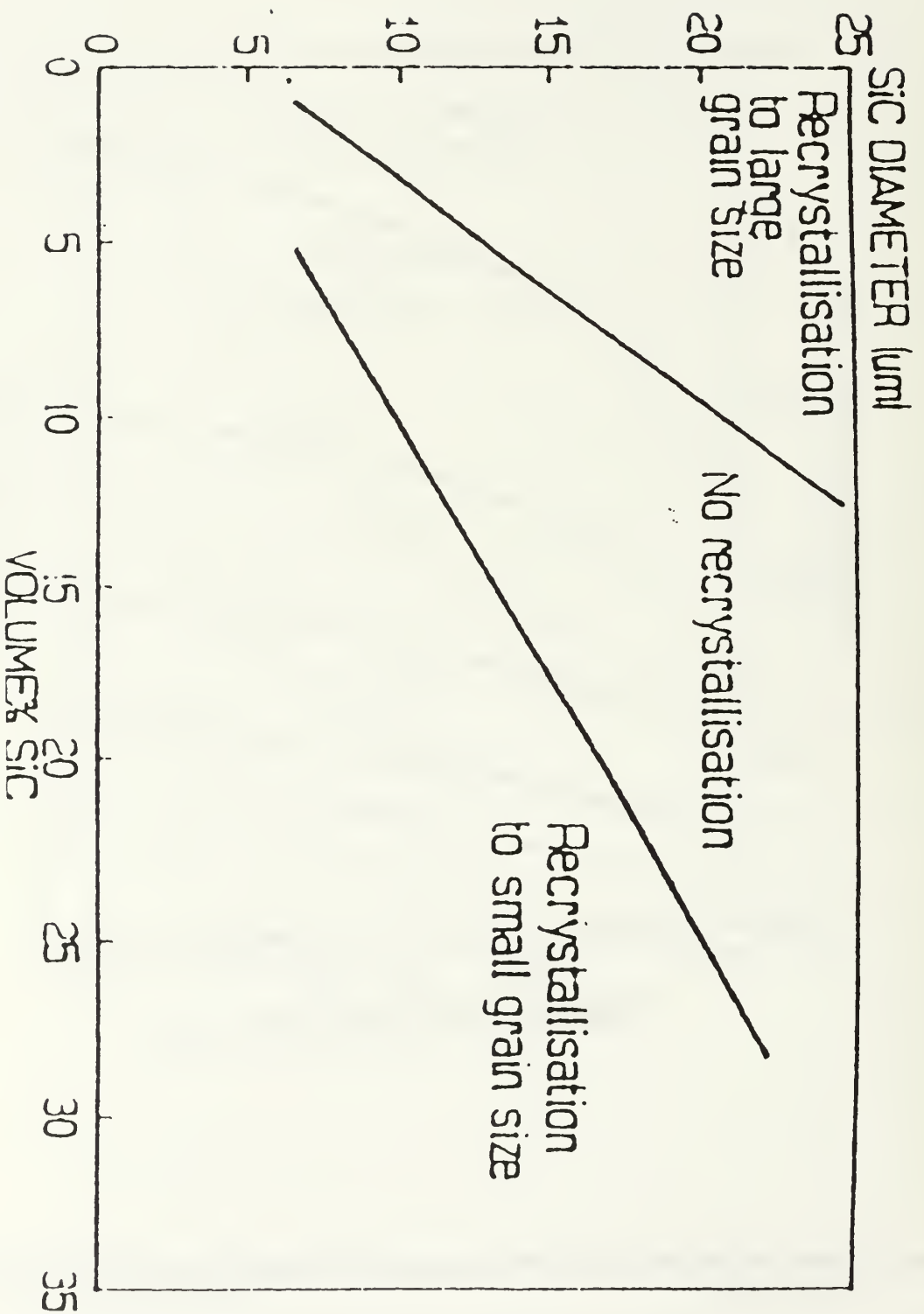


Figure 4: Summary of microstructures developed during hot working. From Reference [3].

volume fractions, recrystallization is more likely to proceed through conventional mechanisms (e.g., grain boundary nucleation). The role of reinforcement volume fraction may be elucidated as follows. At high volume fractions, a large amount of strain may be stored in the matrix since slip is forced to occur next to the hard SiCp to maintain interfacial compatibility, thus enhancing the likelihood of formation of intense deformation zones. Additionally, high reinforcement volume fraction is associated with close particle spacing, which allows for an overlap of deformation zones, thus further encouraging nucleation of recrystallization next to particles [Ref. 3].

Kalu and McNelley [Ref. 4] studied a cast and extruded 6061 Al-Al₂O₃ composite as it progressed through the TMP schedule constituting multiple rolling passes at elevated temperatures. They observed that at higher rolling temperatures, higher strains are required in order to stimulate PSN, see Figure 5 [Ref. 4], presumably because of the operative relaxation mechanisms (such as climb and cross-slip). They also confirmed that during rolling, PSN of recrystallization initiates at the larger reinforcement particles, with progressively smaller particles acting as nucleation sites with increasing rolling strain or increasing number of rolling passes, represented by Figure 6 [Ref. 4].

Xia, Sakaris and McQueen [Ref. 5] studied a 15 vol% SiCp 6061 Al MMC under torsion at elevated temperatures, and observed that it undergoes greater strengthening and work hardening at the lower temperatures. The matrix around the SiCp was observed to develop a much higher dislocation density than that of the normal bulk alloy. It was hypothesized that the high dislocation density regions restricts matrix plastic flow and contributes to the strength and strain hardening [Ref. 5]. This behavior is demonstrated in Figure 7 [Ref. 5]. Furthermore, at temperatures between 200-300°C the SiC particles inhibit climb of dislocations, but as temperatures increase above 300°C the inhibition is significantly diminished [Ref. 5]. These relationships are extremely useful in attempting to understand the processes which are prevalent during extrusion of a DRA composite.

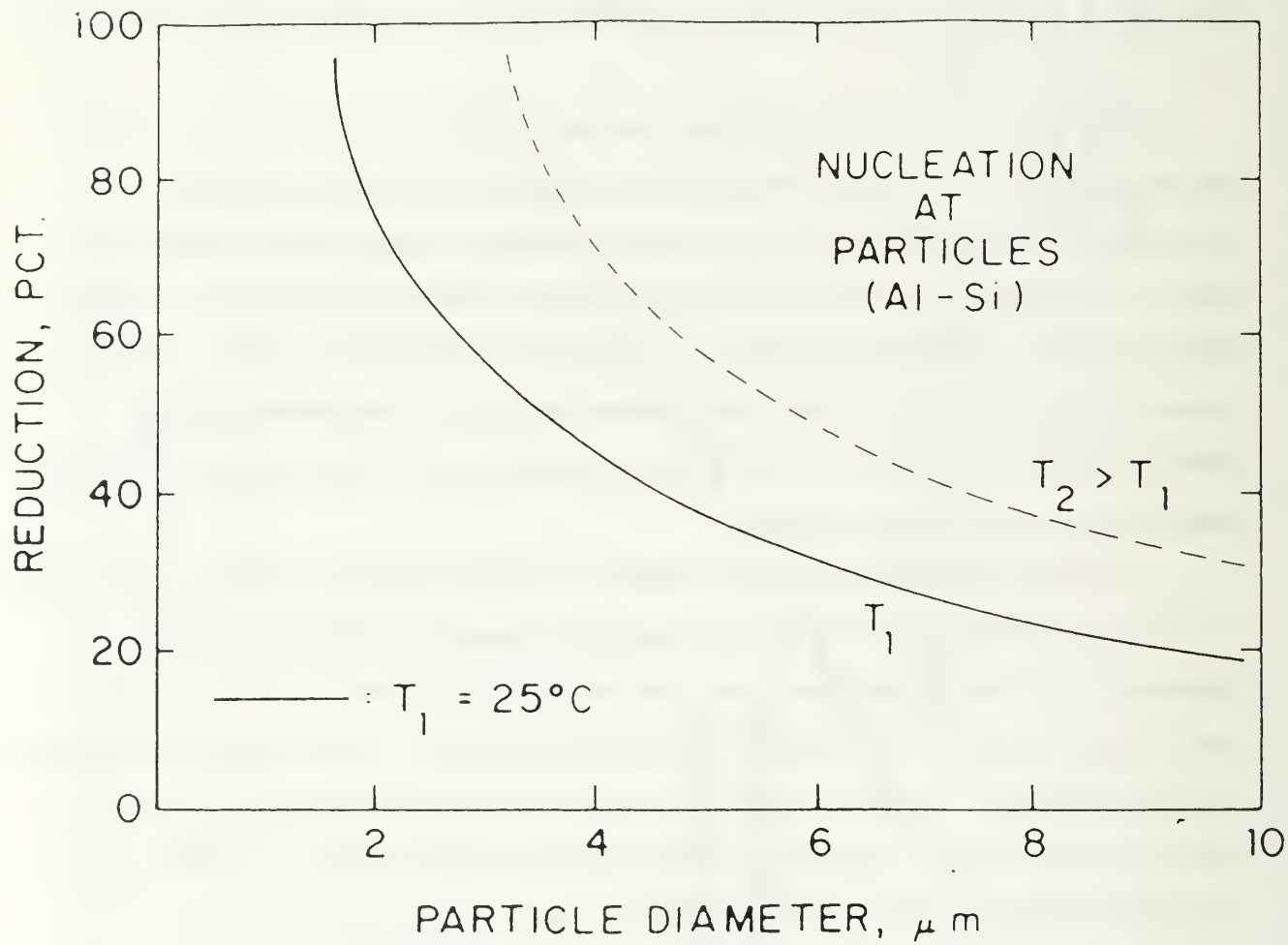


Figure 5: The dependence of PSN on reduction and particle size for Al-Si showing that increased temperature increases the reduction necessary for PSN. From reference [4].

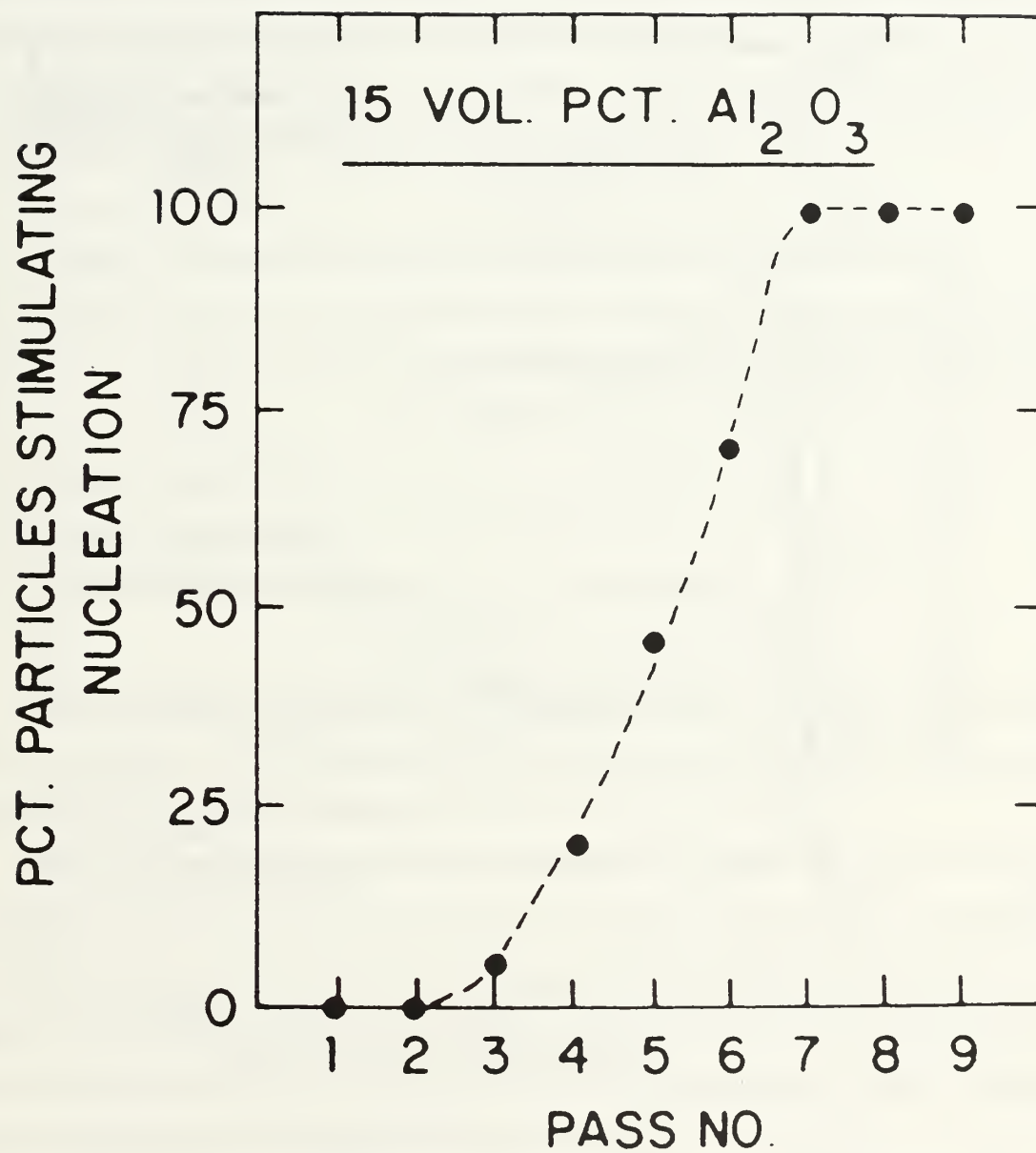


Figure 6: Plot of percentage particles stimulating nucleation of recrystallization versus the number of rolling passes. From Reference [4].

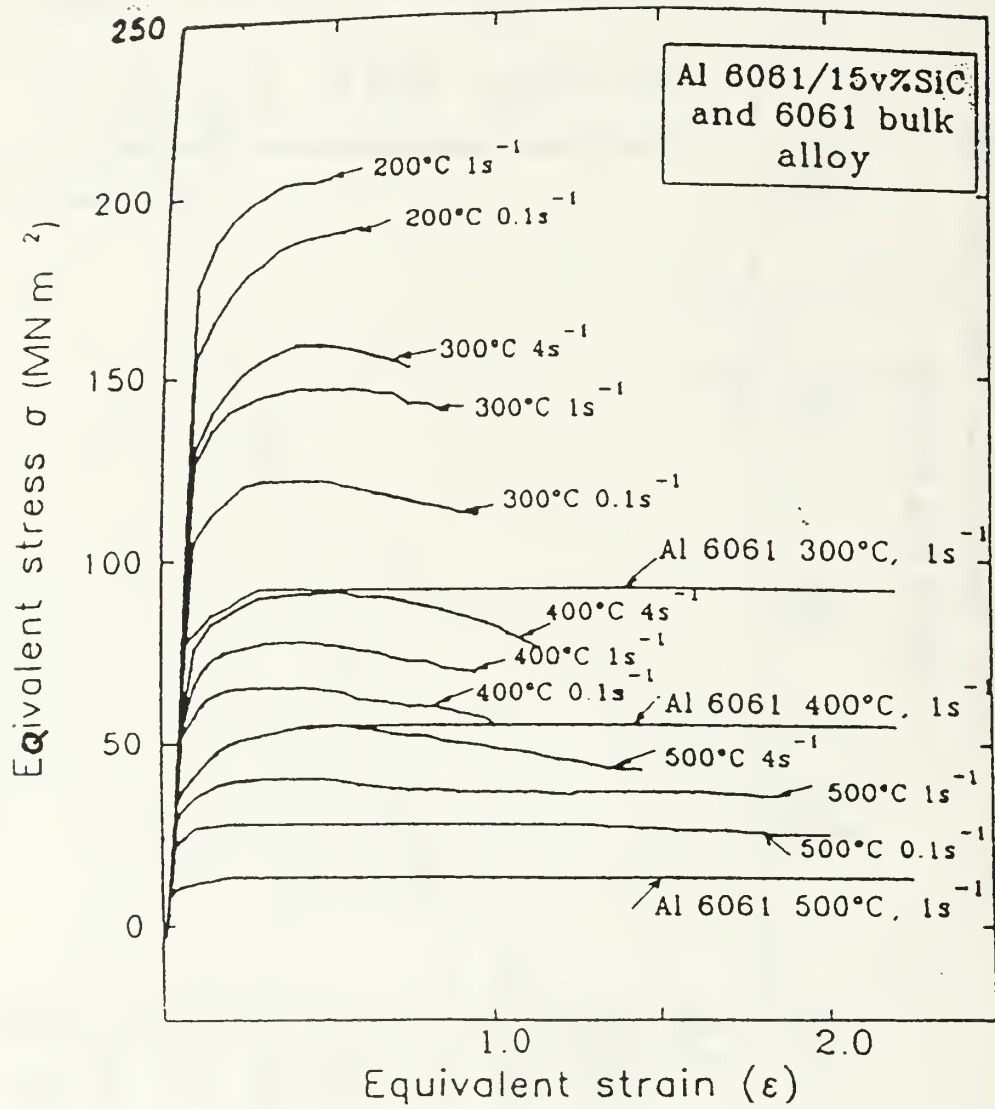


Figure 7: Equivalent stress vs. strain of Al-6061-15 vol% SiCp composite and of 6061 bulk alloy at test temperatures between 200-500°C. From Reference [5].

B. AGING IN Al-Mg-Si ALLOYS AND Al-Mg-Si MATRIX DRA

Differential Scanning Calorimetry (DSC) can be used to determine the precipitation processes operative in age hardenable Al alloys. Figure 8 [Ref. 6] shows the thermogram of a solutionized and quenched monolithic 6061 Al alloy. Previous research for 6XXX alloys was conducted by Dutta and Allen [Ref. 6] where detailed TEM characterization of these peaks was performed for the monolithic Al6061 alloy. They are as follows:

1. peak a - tiny precipitates attributed to the formation of vacancy-Si clusters.
2. peak b - consists of an unresolved doublet of the formation of unresolved shapes of GPI zones (centered at 500 K) and needle-like GPII zones or β'' (centered at 510K).
3. peak c - needle-like β'
4. peak d - plate-shaped β .
5. peak e - the dissolution of β .

Although the peak temperatures and the precipitate volume fractions in the thermograms of a DRA composite varied somewhat from those of the corresponding Al alloy matrix, the basic precipitation processes remained [Ref. 7].

The formation of GPI and GPII zones were found to be parallel competitive processes which relied upon the size and concentration of the Si-vacancy clusters [Ref. 6]. Preaging was found to reduce the number of quenched-in vacancy loops by coalescence, growth and annihilation, thereby promoting the nucleation of needle-like GPII zones in favor of the spherical GPI zones which are favored by high concentration of fine silicon-vacancy clusters. The same behavior was observed in both the monolith and composite.

DRA ages considerably faster than the unreinforced alloy [Ref. 7-12]. This has usually been attributed to the acceleration of both nucleation and growth processes due to the increased dislocation density found in DRA relative to unreinforced alloys.

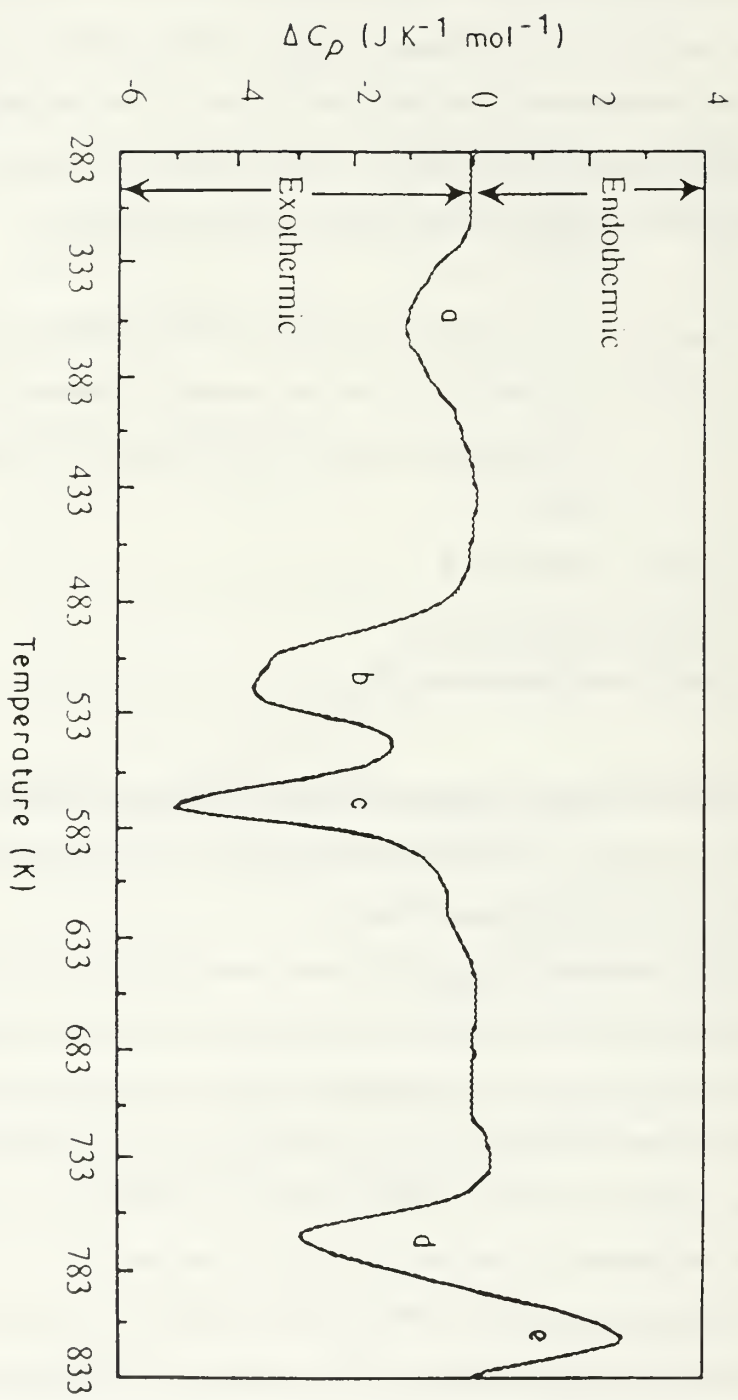


Figure 8: DSC thermogram of solutionized and quenched 6061 Al showing four precipitate formation peaks, a through d, and one dissolution peak, e. From Reference [6].

Three main differences between DRA and monolithic Al are evident:

1. The presence of reinforcements accelerates the overall age hardening behavior of the composite, and in particular, accelerates β' precipitation.
2. As the volume percent of Al_2O_3 increases, less Si clusters are formed during the DSC scan since most clustering occurs during quenching from solution heat treatment.
3. The relative proportion of β' to β is larger in the DRA than in the monolith.

This has been attributed to the stabilization of the strain fields around the semi-coherent β' by the numerous dislocations present in the DRA matrix, thereby reducing the driving force for strain energy reduction by transformation of β' to incoherent β [Ref. 7]. Thus, thermally generated dislocations in the DRA matrix serve to accelerate, as well as stabilize, the β' precipitates which form during age hardening.

C. MECHANISMS OF DEFORMATION AND DAMAGE IN DRA

Fracture modes in DRA are often difficult to determine since there are many factors which contribute to the overall toughness of DRA. The toughness tree, Figure 9 [Ref. 13], outlines the components involved in determining toughness. Of particular interest are the main branches, extrinsic and intrinsic, which represent the separate routes one might take to improve fracture resistance. While extrinsic routes can be utilized selectively to produce composites with very high toughnesses along certain directions, these routes typically render the composite anisotropic, while simultaneously increasing its cost. Therefore, for the majority of applications utilizing the workability, formability and isotropy of DRA, development of intrinsic routes to improve fracture toughness are crucial. This research has focussed on improving the intrinsic

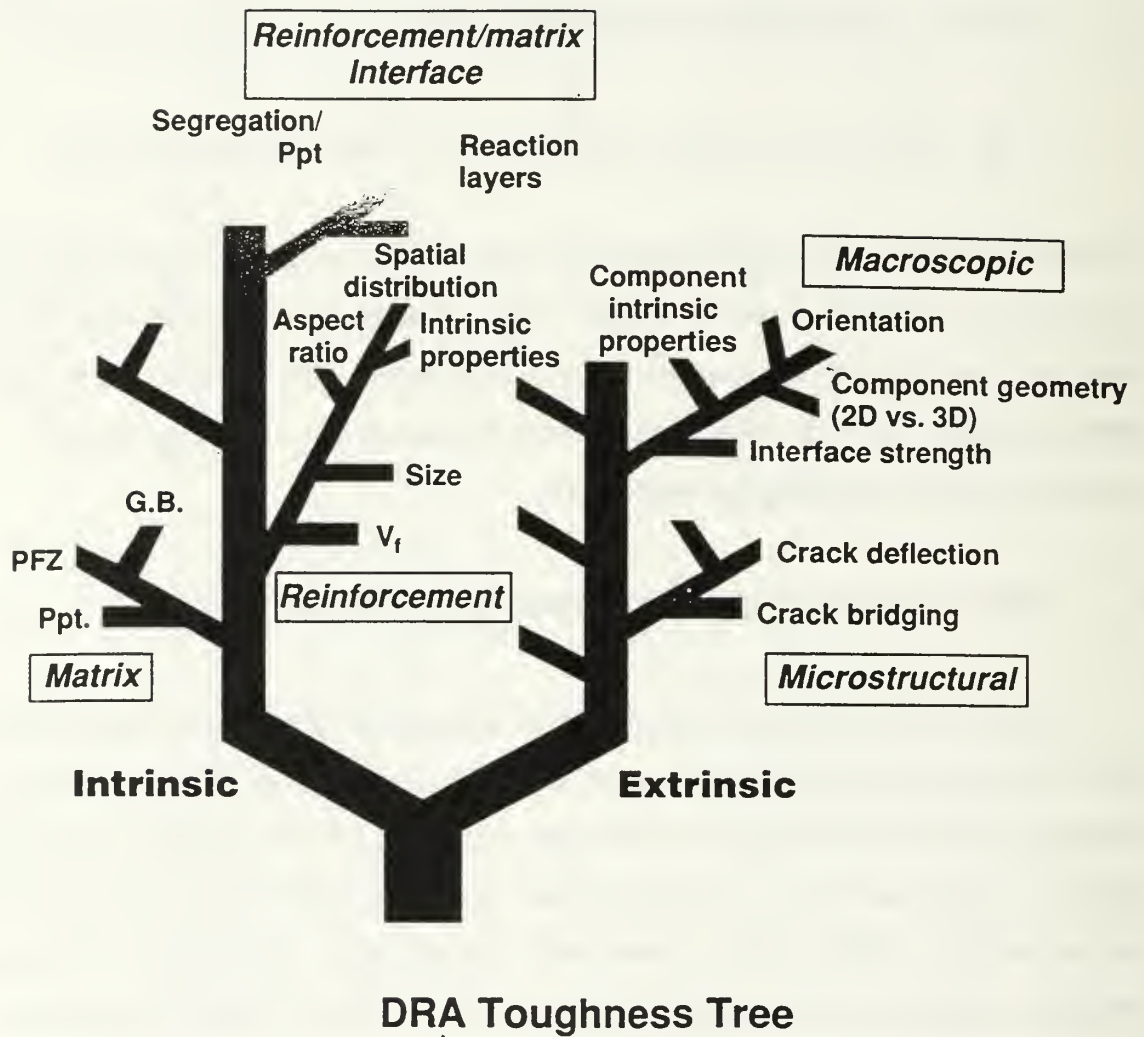


Figure 9: Discontinuous Reinforced Aluminum Toughness Tree which schematically illustrates the many factors which affect toughness for DRA. From reference [13].

fracture toughness of DRA by microstructure control. In particular, effort was made to optimize the particulate distribution and the final matrix grain structure by post-fabrication deformation processing heat treatment.

The predominant mode of failure in DRA is cracking of the particulates followed by linkage in the matrix following matrix deformation. [Ref. 14-16]. The role of particulates in the fracture of metallic materials has been studied in detail by Argon et al. [Ref. 17], and particle-matrix decohesion has been generally thought to be responsible for crack/void initiation. In DRA, crack initiation at the particle-matrix interface has been observed in the overaged state for age hardenable aluminum matrices [Ref. 14], where incoherent precipitates were found to segregate at particulate-matrix interface, and thereby weaken the interface. In addition to particulate fracture and interface decohesion, fracture may also initiate in the matrix and has been detected in regions with large hydrostatic tensile stresses, e.g., within regions with extensive particle clustering [Ref. 16]. Further, the fracture modes in DRA have been observed to be affected significantly by heat treatment [Ref. 13].

D. INTRINSIC PARAMETERS AFFECTING FRACTURE RESPONSE

1. The Reinforcement

The manipulation and control of the quality, size, distribution and shape of reinforcement materials can inherently affect the performance of DRA. Particulate volume fraction plays an important role not only in determining the mechanical properties of the composite such as strength and stiffness, but also in the recrystallization of the matrix by PSN during post-fabrication thermo-mechanical processing. As indicated earlier, finer grains are achieved with higher volume fractions and smaller particles. But larger particles are more likely to stimulate recrystallization. Therefore, a balance between particle size and volume fraction is necessary when considering TMP and PSN.

In general, increasing particulate volume fraction, while enhancing stiffness and strength, results in reduced fracture toughness of DRA. The effect of volume fraction on toughness tends

to be strongest at lower volume fractions and decrease with increasing volume fraction , Figure 10 [Ref. 13,18]

Particle size tends to have negligible effect on the fracture toughness-yield strength relationship. However, the toughness-tensile strength relationship favors finer particle sizes, as revealed in Figures 10-11 [Ref. 13,18]. Finer reinforcements possess less cracked particles than larger reinforcement, allowing a greater extent of matrix work hardening prior to particulate fracture [Ref. 19], thus allowing the composite to attain higher ultimate tensile strengths. Consequently, there appear to be two factors which counteract each other when altering particle size and volume fractions. Achieving fine grains with particles large enough to stimulate PSN but small enough to satisfy the natural tensile strength-fracture toughness relationship requires careful consideration. Additionally, a balance between the high volume fraction required for PSN and those shown in Figure 10 [Ref. 13,18] must be maintained.

The type and quality of reinforcement particles have been studied [Ref. 13] and it was found that Al_2O_3 and SiC particles have the highest resistance to fracture when embedded in an Al matrix, especially when compared to the alloying element Si which is typically present in most cast Al matrices [Ref. 20].

The effects of spatial distribution has been considered revealing regions of particle clustering severely influence the fracture resistance of DRA. These areas negatively affect toughness and provide paths for linkage of the damage [Ref. 14-16]. The fracture which initiates within this cluster is normally due to either particle cracking or particle/matrix decohesion whereby final fracture is achieved through matrix failure inbetween the closely spaced particles. Moreover, the failure process is controlled by the large triaxial stress intensification exerted on the matrix within these clusters by the constraints of the surrounding elastic particles [Ref. 16]. This has been confirmed through the observation of increased tensile ductility when DRA was loaded under a superimposed hydrostatic pressure [Ref. 19]. The particle distribution can be improved through TMP as previously mentioned which ultimately can lead to an increase in tensile ductility [Ref. 1] and fracture resistance [Ref. 21] due to the more uniform spatial distribution of the reinforcement.

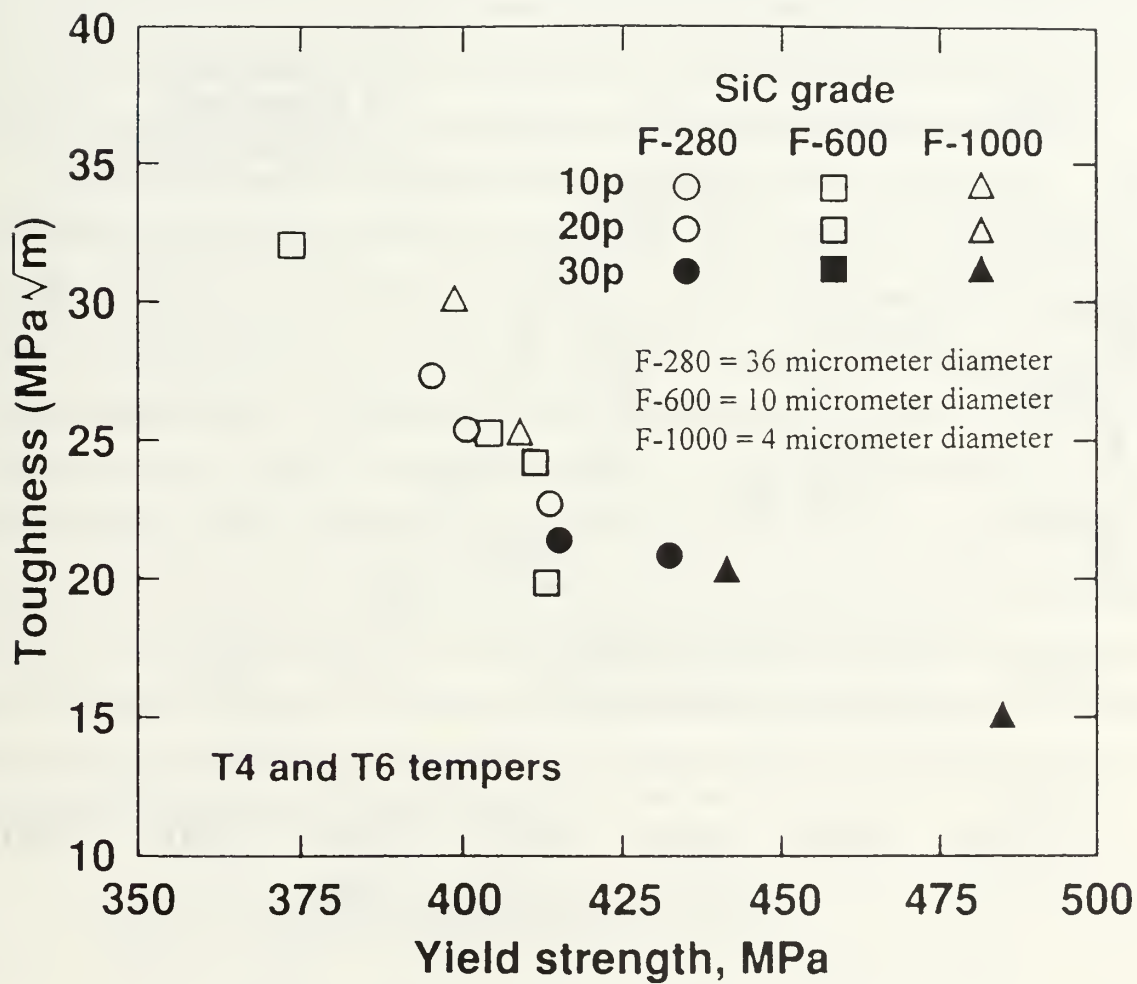


Figure 10: Toughness-yield strength relationship for DRA materials in which particle volume % and size are varied. From Reference [13, 18].

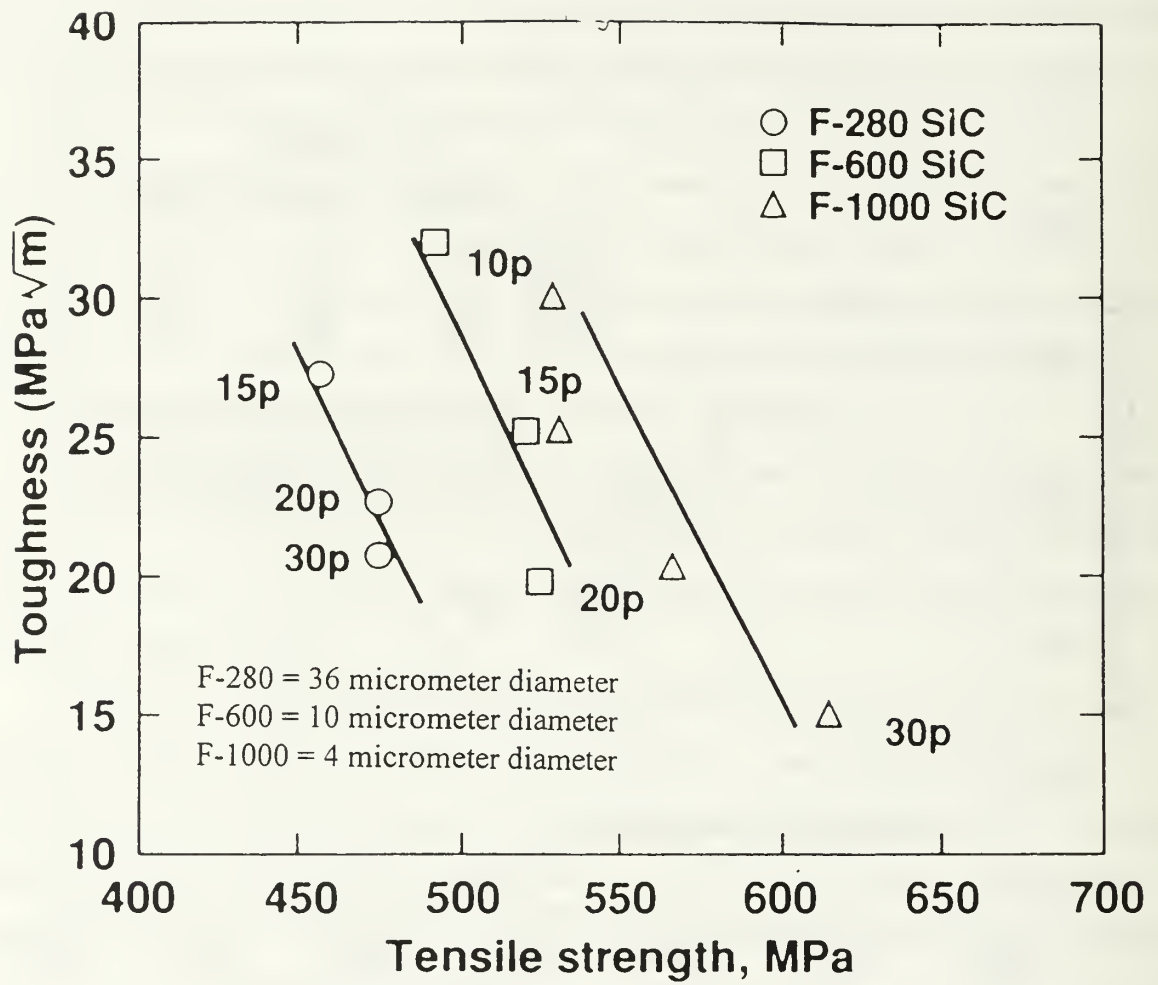


Figure 11: Toughness-tensile strength relationship for DRA materials demonstrating the effect of particle size. From Reference [13].

2. The Matrix

The matrix plays a vital role in determining the fracture toughness of DRA. Figure 12 [Ref. 13] presents this issue clearly for similar manufacturing processes (P/M) and volume fractions. The differentiating parameters were heat treatments and alloy composition. Figure 13 [Ref. 13,18] reveals the wide range of results which can be achieved through the variation of matrix material. Therefore, various manufacturers have produced alloys which are particularly useful and specifically designed for employment in DRA materials, 6092 Al included.

In addition to matrix composition, the heat treatment condition of the matrix (precipitation hardening for age hardenable matrices) has a strong impact on the fracture properties of DRA. In heat treatable aluminum alloys, tensile ductility and fracture toughness decrease while aging from the solution treated condition to peak strength, but increase again with increasing overaging. In DRA, however, this phenomenon is not observed. Figure 14 [Ref. 14] demonstrates that in the overaged (OA) condition the decrease in tensile strength is associated with a decrease in fracture toughness, although tensile ductility usually increases on overaging. This decrease in toughness has been attributed to the presence of incoherent particles, which serve as additional sites where damage initiation can occur. Further during overaging, some precipitate segregation was observed at the reinforcement-matrix interface, along with a greater degree of interface failure during fracture, suggesting that such segregation may be instrumental in weakening the interface [Ref. 14].

3. The Reinforcement-Matrix Interface

Argon Im, and Safoglu have derived approximate solutions for maximum interfacial stress for equiaxed particles and for internal concentration of stress inside elongated particles in a pure shear field [Ref. 22]. These analyses were based on the assumption that the plastic resistance of the matrix will increase with strain hardening. Eventually, a steady state must exist where the local interface stress relates to the resistance of the surrounding field by a constant multiple leading to a constant stress intensity [Ref. 17].

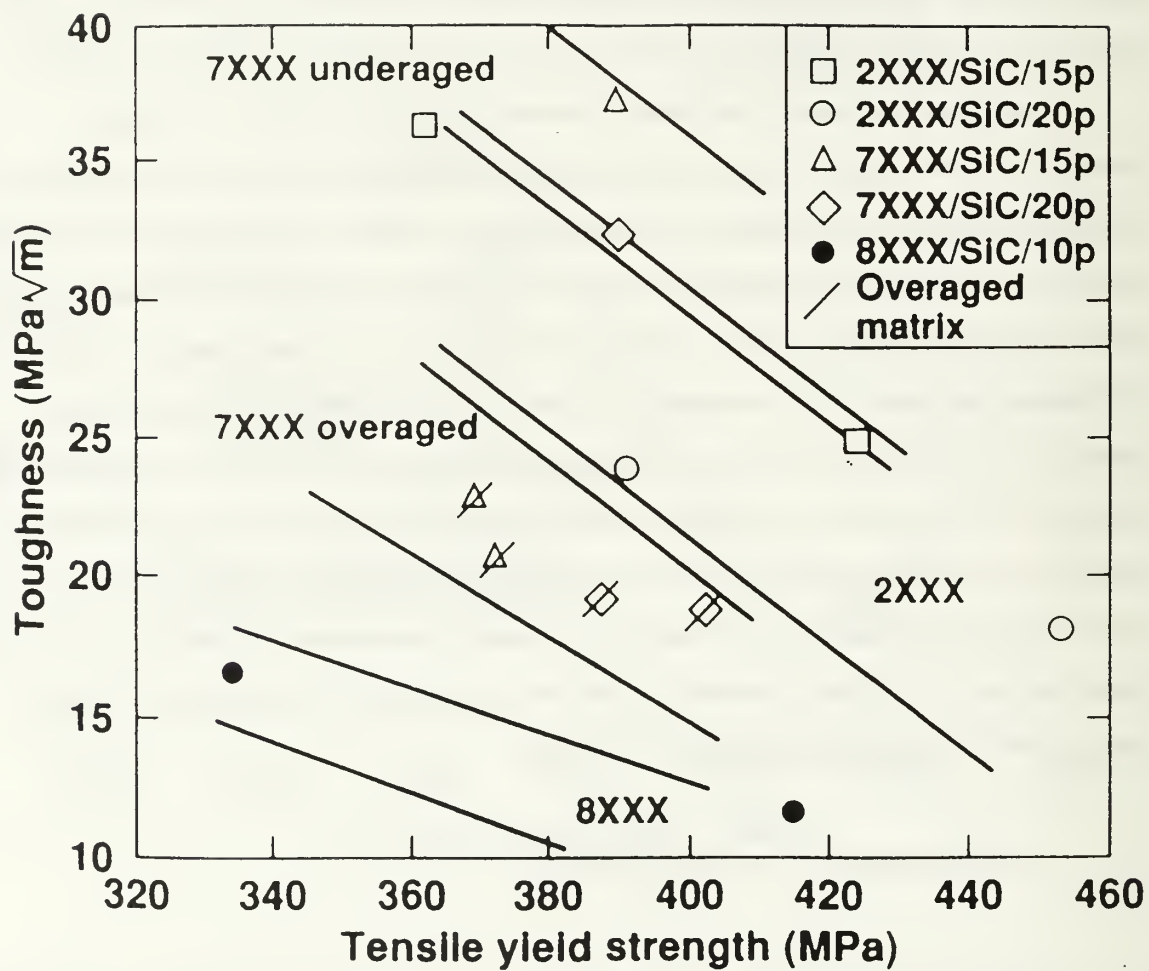


Figure 12: Toughness-yield strength relationships for a range of SiC particulate-reinforced DRA materials highlighting the matrix effect. From Reference [13, 18]

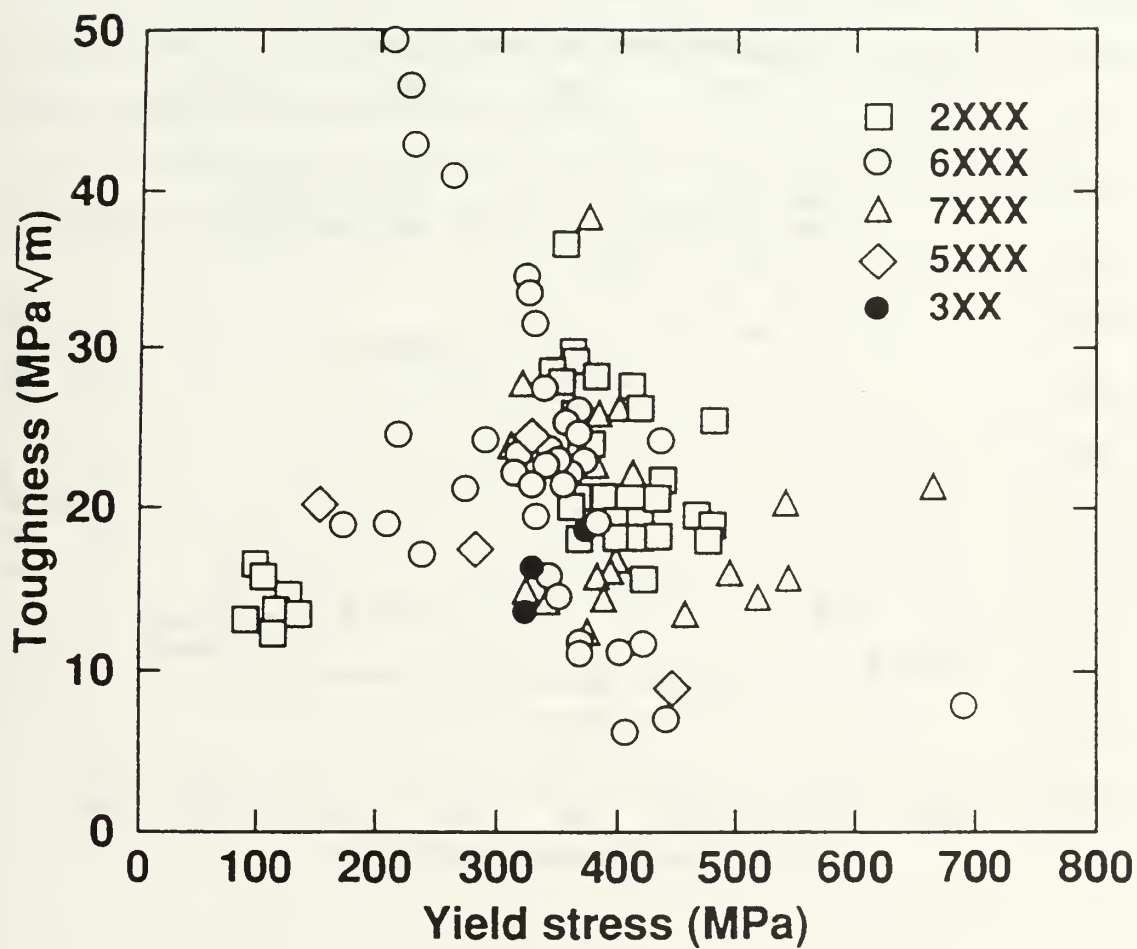


Figure 13: Toughness-yield strength relationship for a number of DRA materials illustrating the wide range of performance. From Reference [13,18].

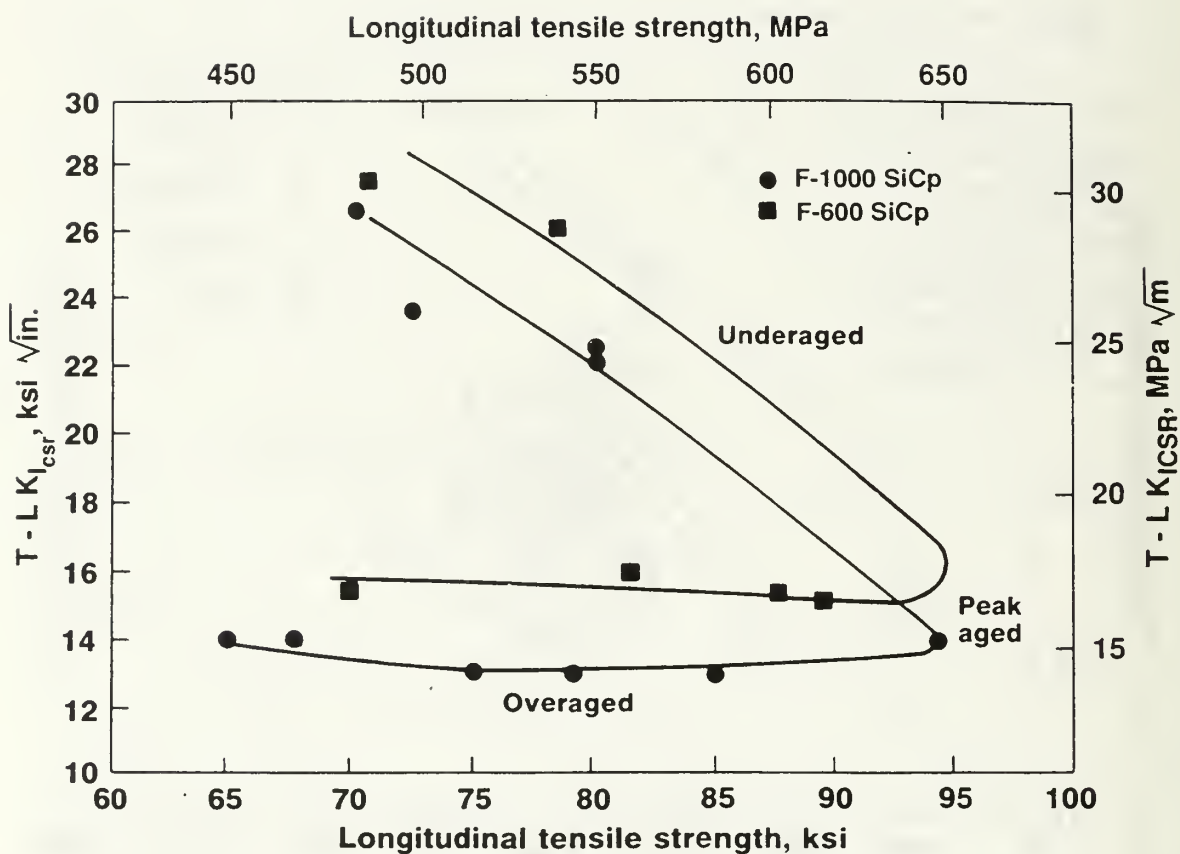


Figure 14: Toughness-tensile strength relationship for 7XXX/SiCp/15p DRA materials illustrating the influence of matrix aging condition. From Reference [13-14].

Two particle size effects were found to exist. Small particles cannot nucleate a cavity surrounding the particle matrix interface because the strain energy stored around them is insufficient to compensate for producing the surface energy associated with cavity formation. Conversely, large particles tend to nucleate more cavities as explained through the particle interaction effect in a randomly dispersed field of particles with broad size distribution. Whereby, a significant probability exists where two larger than normal particles are neighbors at a spacing less-than-average resulting in an increase in interfacial stresses due to interpenetration of plastic zones around the particles [Ref. 17,22] .

In conclusion, fracture toughness is a function of particle distribution, matrix microstructure, matrix and particle properties and interfacial strength.

III. EXPERIMENTAL PROCEDURE

A. MATERIAL

The material used for the present work comprised a 17.5 volume percent SiCp reinforced 6092 Al composite, which was manufactured by DWA Composites, Chatsworth, CA, via the powder metallurgy (P/M) route. The composition of the matrix alloy, Al 6092, is as follows (in weight percent) :

Si	Mg	Cu	Mn	Cr	Zn
0.4-0.8	0.8-1.2	0.7-1.0	0.15max	0.15max	0.25max
Ti	Fe	O	Others, each	Al	
0.15max	0.7max	0.05-0.5	0.05 max	remainder	

The composite was consolidated in the form of 45.72 cm (18 inches) diameter billets, which were subjected to two extrusion steps by DWA Composites before being supplied. The primary extrusion was conducted at 370-450°C using shear-faced dies to reduce the billet diameter to 20.32 cm (8 inches). This was followed by a secondary extrusion wherein the diameter was further reduced to 8.89 cm (3.5 inches) at 450-565°C using conical dies. The resulting total true extrusion strain of the composite in the as-received condition was 3.38.

B. PROCESSING

The as-received composite was subjected to one final extrusion step at Wright Laboratory, Wright Patterson Air Force Base, Ohio, whereby this comprised reduction of the 8.89 cm (3.5 inches) diameter billet to a rectangular billet of 1.27 cm x 3.81 cm (0.5" x 1.5") cross section under one of the three following conditions.

Sample Id	Extrusion Temp (°C)	Extrusion Rate (strain/second)	PSN expected
13184	450	5.6/s	maybe
13185	400	5.6/s	yes
13186	400	0.56/s	no

All extrusions produced a total final true strain of 5.83. The total strain was maintained at this level since this strain was found to be adequate to redistribute all the reinforcement particulates to the maximum extent possible, thereby producing a homogeneous reinforcement distribution in all composites. Thus having eliminated variations in particle distribution, the primary variable parameter in the composites with the three different extrusion conditions was the matrix microstructure, and in particular, the grain size and structure.

Particle stimulated nucleation of recrystallization was expected to occur in sample set 13185, which was processed well within the PSN regime of temperature and strain rate; PSN was not expected in 13186; whereas sample set 13184 was processed near the border of the PSN and non-PSN regimes. As indicated earlier, the basis of PSN is to strain the material as highly, at as high a strain rate, and at as low a temperature, as possible. The low temperature and high strain rate safeguard against the occurrence of recovery. Instead, severe lattice rotations are formed adjacent to the undeformable SiCp. Consequently, dislocations are less likely to climb and will pile up at the SiCp. The associated strain energy will provide the driving force for PSN during subsequent annealing. However, the likelihood of dynamic recrystallization remains during the extrusion process. Figure 3 [Ref. 3], which shows the critical temperatures below which adequate lattice rotations occur in a DRA (with 6-7 micrometer sized particles) to result in PSN of recrystallization, provides the basis for selection of the temperature - strain rate regimes for the extrusion processes.

C. MECHANICAL TESTING/SAMPLE PREPARATION

Following extrusion, Compact Tension (CT) and Tensile samples were manufactured in accordance with Figures 15-16. Care was taken, during the manufacturing process, to ensure that the tensile and CT samples were manufactured such that their loading and extrusion directions remained parallel.

The initial notch in the Compact Tension (CT) specimens were produced via electric discharge machining (EDM) using a 250 micrometer (0.01 inch) diameter Cu-Ni wire. Following any required heat treatment, the notch was extended using a high speed wire saw equipped with a 25 micron (0.001 inch) diameter carrier wire in conjunction with 1-6 micron Boron Nitride powder suspended in water. This notch extension technique was utilized in lieu of fatigue precracking the fracture samples, and has been verified to be satisfactory for DRA materials [Ref. 15]. All initial crack length to specimen width ratios (a_0/w) were between 0.5 and 0.6. The initial crack length, a_0 , is determined in accordance with the ASTM standard where following fracture, the broken specimen is measured at nine equally spaced points centered about the specimen centerline by: averaging the two near surface measurements, combine the result with the remaining seven crack length measurements and determine the average. The difference between any of the seven additional crack measurements shall not exceed 10% of the averaged near surface lengths. (ASTM E399 and E813-89).

Double notched tensile samples were employed to determine failure mechanisms in composites subjected to two highly dissimilar heat treatment conditions following extrusion (artificially aged at 170°C for 8 hours following solution treatment at 560°C for 1.5 hours, and annealed for 20 minutes at 450°C following extrusion) matrices. These samples were used to identify microstructural features responsible for fracture initiation. While one notch would ultimately fail, the remaining notch would be prepared for optical microscopy and mounted to reveal a profile view, of the unfailed and failed regions, with the intent of exposing the sites of fracture initiation. Additionally, the other half of the failed tensile specimen was mounted for fractography analysis on the Scanning Electron Microscope (SEM).

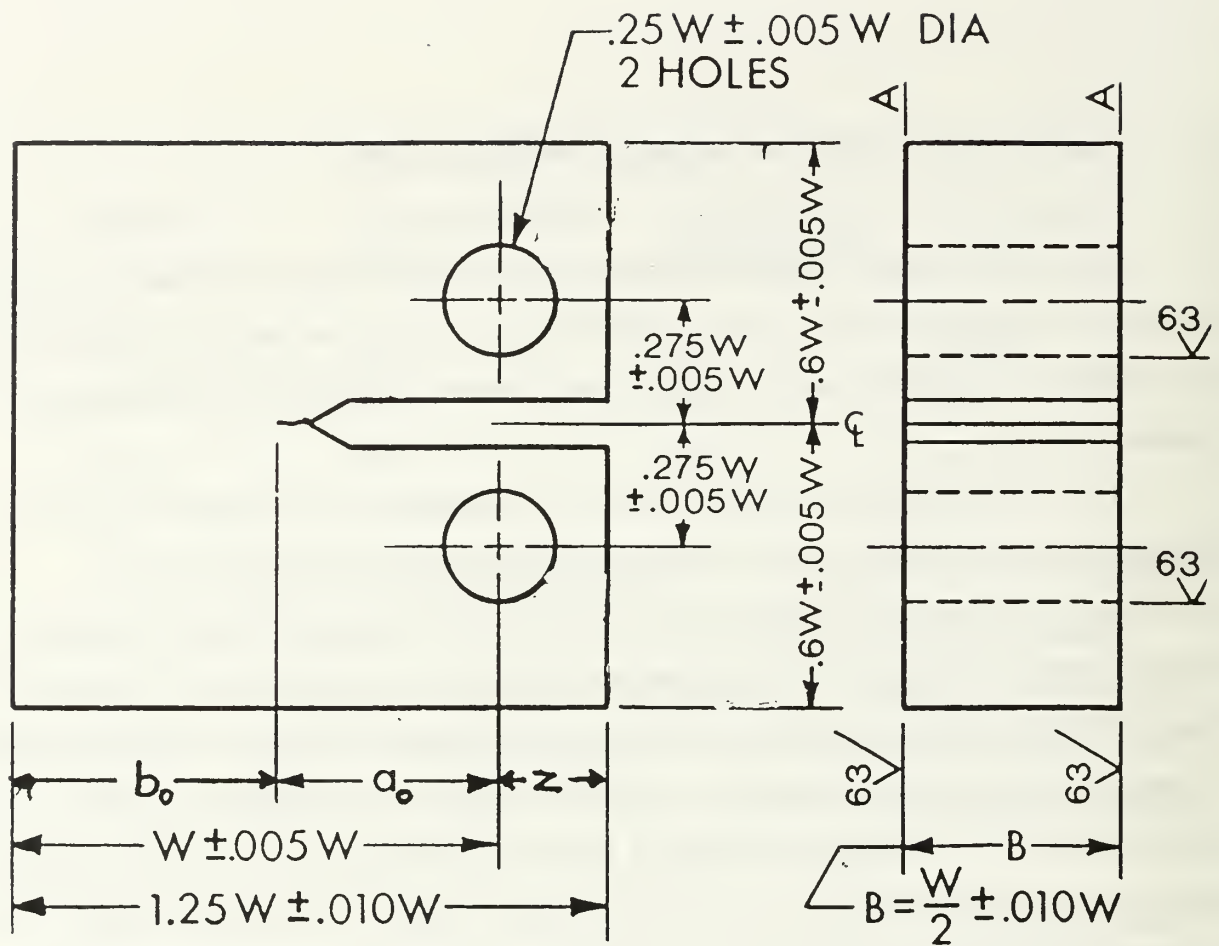


Figure 15: Compact Tension (CT) Specimen in accordance with ASTM E399 and ASTM E813-89.

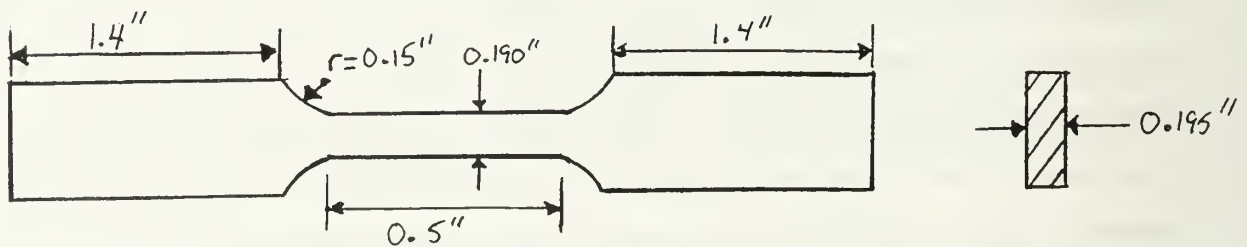


Figure 16: Tensile Specimen used to obtain mechanical properties of DRA.

Both notches were fabricated with the use of a wire EDM. The depths were controlled through the use of a micrometer, to approximately 1/4 the specimen width, see Figure 17, and care was taken to ensure that the remaining ligaments of both notched regions were of the same length.

DSC samples, 5.5 mm in diameter and about 2 mm thick, were bored out of composite sheets of the same thickness using the EDM in conjunction with a hollow cylindrical brass electrode. Following sample manufacture, the DSC specimens were ground, heat treated and water quenched. Prior to DSC scan, the specimens were weighed and encapsulated in an aluminum pan.

All samples, including DSC specimens, were then heat treated to various conditions which covered a wide spectrum of expected grain and precipitate structures. These heat treatments, imparted to the materials following extrusion, comprised the following. The designations used to describe these heat treatment conditions are given in the parentheses.

1. Solution treatment at 560°C for 1.5 hr. + artificial aging at 170°C for 8 hrs (-T6)
2. Solution treatment at 560°C for 1.5 hr. + natural aging for 9 months (-T4)
3. Static annealing at 450°C for 20 minutes (-450)
4. Static annealing at 480°C for 20 minutes (-480)
5. Static annealing at 450°C for 20 minutes + artificial aging at 170°C for 8 hrs.
(-450-170)
6. Static annealing at 480°C for 20 minutes + artificial aging at 170°C for 8 hrs.
(-480-170)
7. Solution treatment at 560°C for 1.5 hr. + static annealing at 450°C for 20 minutes + artificial aging at 170°C for 8 hrs (-560-450-170)

Each heat treatment was concluded with a rapid cold water quench.

DSC experiments were conducted on a Perkin-Elmer 7 Series Thermal Analysis System at a scan rate of 10° C/min over a range of 40-540°C. The detailed procedure used in the DSC studies are given elsewhere [Ref. 7].

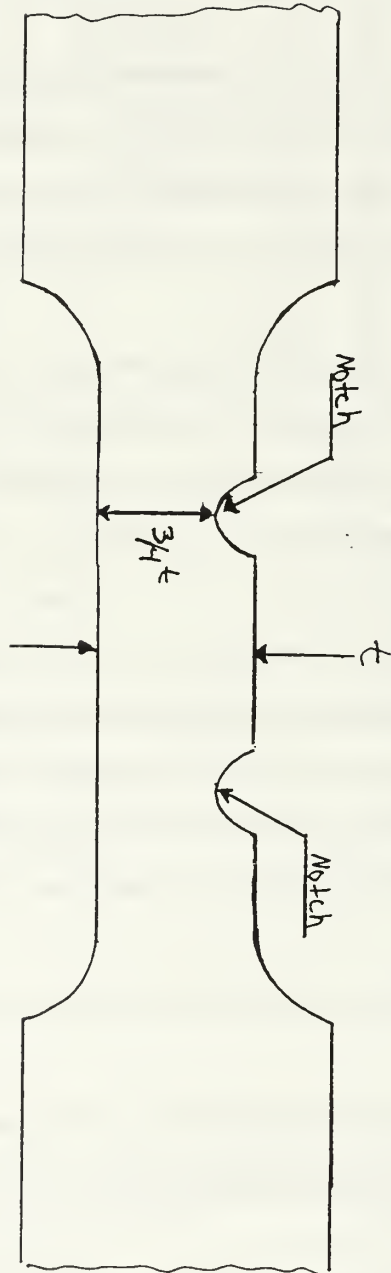


Figure 17: Double notched tensile specimens used to determine mode of fracture.

D. POLISHING SCHEDULE

The following schedule was used for polishing the metallographic samples of the double notched samples to reveal the crack profiles after sectioning. The schedule was borrowed from Buehler Corporation and found to work extremely well. All polishing was completed on a Buehler Ecomet 3 Variable Speed Grinder/Polisher. See Table I.

E. TESTING

The CT and tensile samples were tested at room temperature utilizing a MTS 8010 Servo Hydraulic mechanical test system. Tensile tests were conducted in displacement control at a rate of 3mm/minute, and 0.2% offset yield strength, ultimate strength and % elongation were obtained. CT specimens were manually tested in load control utilizing the single specimen compliance method in accordance with ASTM E813-89.

Data was recorded continuously with a Hewlett Packard XY Recorder and digitally, every second, on an Apple Macintosh based data acquisition system using Strawberry Tree Software.

The specific dimensions and requirements for the manufacture and use of the clevis grips and clip gage, outlined in ASTM 399 and ASTM 813-89, was strictly adhered to.

F. INTERPRETATION AND ANALYSIS OF RESULTS

Clip gage displacements were then converted to load line displacements for use in accordance with ASTM 813-89. Rao and Acharya [Ref. 23-24] provide a reasonable method to convert clip gage displacements to load line displacements which introduce error of no more than 10% [Ref. 23-24]. Therefore, simpler machining and better accessibility of the knife edges, necessary for clip gage placement, is achieved. Additional research [Ref. 23-26] has established that this approach provides a good alternative to the direct measurement of load line displacement during J-integral testing.

The Rao and Acharya method accounts for various uncertainties in testing; therefore an

TABLE I -SPECIMEN POLISHING ABRASIVE SCHEDULE

Step Number	Polishing Medium	Grit Size	Grit Dia(microns)	Time (min)	Wheel(Rpm)	Comments
1	Carbide Paper	230	46	0.5	12" dia/300rpm	1-5 lbf
2	Carbide Paper	500	30	0.5	12" dia/300 rpm	1-3 lbf
3	Carbide Paper	1000	18	2	12" dia/300 rpm	1-3 lbf
4	Carbide Paper	2400	10	3	12" dia/300 rpm	1-3 lbf
5	Carbide Paper	4000	5	3	12" dia/300 rpm	1-3 lbf
6	diamond spray w/ Metadi extender Chemomet cloth		6	6 to 9	12" dia/250 rpm	1-3 lbf
7	diamond spray w/ Metadi extender Microcloth		1	6 to 9	12" dia/250 rpm	1 lbf
8	Coloidal Silica w/ Microcloth		0.05	1	12" dia/250 rpm	1 lbg

effective modulus, E_M is calculated in terms of clip gage displacement (V_g). This relationship is quite useful, since ASTM 813-89 uses an effective modulus in terms of load line displacement (V_{II}). These two quantities are different and must be separately calculated when calculating J_{Ic} in accordance with ASTM 813-89. Nevertheless, E_M can be determined from [Ref. 24]:

$$\frac{E_M BV}{P_o} \varepsilon = (1 + 0.25/\eta_0) \frac{(1 + \eta_0)^2}{(1 - \eta_0)^2} [1.6137 + 12.678\eta_0 - 14.231\eta_0^2 - 16.61\eta_0^3 + 35.05\eta_0^4 - 14.494\eta_0^5] \quad (3)$$

where $\eta_0 = a_0/w$, a_0 is initial crack length, w is the width of the CT, B is the thickness and P_o is the load corresponding to V_g in the linear portion of the load vs clip gage displacement curve obtained experimentally.

For each experimentally determined point of Load (P) and V_g the corresponding crack length must be calculated from the following Equation [Ref. 24]:

$$a/w = 1.001 - 4.6695z + 18.46z^2 - 236.82z^3 + 1214.9z^4 - 2143z^5 \quad (4)$$

where

$$z = \frac{1}{1 + \sqrt{\frac{E_M BV_g}{P}}} \quad (5)$$

The crack size a corresponding to the ($V_g P$) on the experimental curve is then used in the following Equation to convert V_g to V_{II} [Ref. 24]:

$$V_a = \frac{\sqrt{\frac{a^2 + w^2}{2}}}{Z + \sqrt{\frac{a^2 + w^2}{2}}} V_g \quad (6)$$

where Z , see Figure 15, is the distance from the load line to the point of the front face displacement measurement.

This procedure then generates a P vs. V_{II} plot which can be used to determine J_{Ic} in accordance with ASTM 813-89. An easier method was recommended by Orange where the conversion factor was determined from extensive experimental data (ref 6 in Archarya paper). The relationship is as follows [Ref. 25]:

$$V_{II}=0.773V_g \quad (7)$$

An error of 1% is experienced over the range $0.35 < a/w < 0.8$. Figure 18 [Ref. 24] compares Orange's results to Archarya's and Rao's formulation, proving the effectiveness of each method when compared to experimental results [Ref. 27]. For J_{Ic} calculation in this research, Rao's and Archarya's method was used.

K_{Ic} for specimens which failed catastrophically was determined in accordance with ASTM E399.

G. DETERMINATION OF J_{Ic} FROM LOAD-DISPLACEMENT RECORD IN THE ABSENCE OF UNLOADING COMPLIANCES

Shih German and Kumar [Ref. 28] have developed formulas for the numerical calculation of the J Resistance curves vital in evaluating J_{Ic} . This formulation has been extremely useful in determining the JR curve when the initial unloading compliances are unreliable or unable to be ascertained. Additionally, all J controlled crack propagation results were primarily calculated in accordance with ASTM 813-89 and checked with the method outlined in reference 28. Overall, the results were in good agreement with the ASTM, with only, at most a 1-2 kJ/m² point difference in J_{Ic} .

Prior to utilizing this method a few constants must be determined from a tensile test. The Osgood-Ramberg stress strain law was utilized to determine the constant, namely alpha and n, where [Ref. 28]:

$$\epsilon/\epsilon_0 = \sigma/\sigma_{YS} + \alpha(\sigma/\sigma_{YS})^n \quad (8)$$

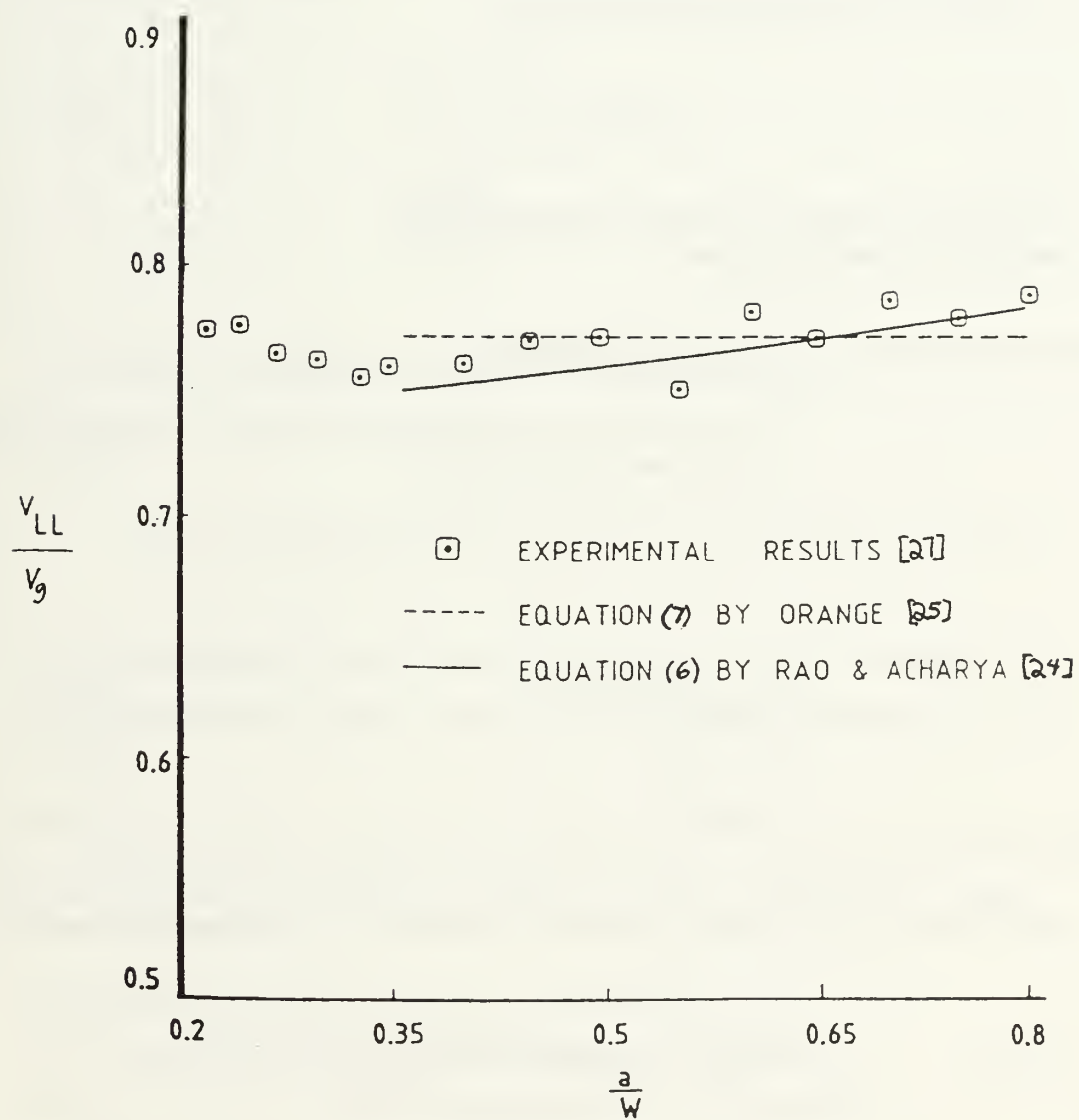


Figure 18: Comparison of analytical and experimental results for the ratio of load line to clip gage displacements (V_{LL}/V_g) vs. crack length to width ratio (a/w) of CT specimen. From Reference [24].

where:

σ_{YS} = materials yield stress

σ = all values of stress obtained from tensile test exceeding σ_{YS}

α = material proportionality constant which compensates for the omission of all data prior σ_{YS}

ϵ = strain at corresponding stresses above σ_{YS} .

$$\epsilon_0 = E \sigma_{YS} \quad (9)$$

E = Young's Modulus as calculated from tensile test

n = strain hardening coefficient

A simpler form of the previous Equation is as follows:

$$\ln(\epsilon_{PL}/\epsilon_0) = n \ln(\sigma/\sigma_{YS}) + \ln(\alpha) \quad (10)$$

or

$$(\epsilon_{PL}/\epsilon_0) = \alpha (\sigma/\sigma_{YS})^n \quad (11)$$

$$\epsilon_{PL} = \epsilon - \epsilon_{EL} \quad (12)$$

$$\epsilon_{EL} = \sigma/E \quad (13)$$

The formulas derived by Shih, Kumar and German for use in determining J are [Ref. 28]:

$$J = f_1(a_E) * P'^2/E' + \alpha \sigma_{YS} \epsilon_0 b h_1(a/w, n) * (P'/P_0)^{n+1} \quad (14)$$

$$V_g = f_2(a_E) * P'/E' + \alpha \epsilon_0 * a * h_2(a/w, n) * (P'/P_0)^n \quad (15)$$

$$V_{II} = f_3(a_E) * P'/E' + \alpha \epsilon_0 * a * h_3(a/w, n) * (P'/P_0)^n \quad (16)$$

where the first term of each Equation is the elastic contribution and the second term consists of the plastic contribution of J , V_g and V_{II} .

Additionally:

$$P'=P/B \quad (17)$$

$$E'=E_{MM}/(1-\nu^2) \quad (18)$$

ν =poissons ratio

E_{MM} =Effective modulus determined from ASTM 813-89 formulation.

a_E =adjusted crack length

$$\epsilon_{00}=\sigma_{YS}/E_{MM} \quad (19)$$

$$f_1=a_E * F1^{1/2}/w^2 \quad (20)$$

$$f_2=V1 \quad (21)$$

$$f_3=V3 \quad (22)$$

$F1$, $V1$ and $V2$ are graphically available in reference [Ref. 29].

An easier form of $F1$ is provided in reference [Ref. 29] of the form:

$$F1=29.6-185.5*a_E/w+655.7*(a_E/w)^2-1017*(a_E/w)^3+638.9*(a_E/w)^4 \quad (23)$$

$V1$ =dimensionless clip gage parameter for the front face displacement [Ref. 29].

$V2$ =dimensionless clip gage parameter for the load line displacement [Ref. 29].

$V1$ and $V2$ were also listed in reference 30 in tabular form where the liberty was taken here to interpret and fit this data into a 6th order polynomial for use in computer code, where:

$$V1= 44444(a_E/w)^6-114153.85(a_E/w)^5+12432.6(a_E/w)^4 \\ -72137.7(a_E/w)^3+23485(a_E/w)^2-3985.9(a_E/w)+289.9 \quad (24)$$

$$V2= -237.037(a_E/w)^6+8485.47(a_E/w)^5-15414.47(a_E/w)^4 \\ +11931.8(a_E/w)^3-4607.8(a_E/w)^2+941.08(a_E/w)-70.81 \quad (25)$$

additionally;

$$a_E = a + \phi r_Y \quad (26)$$

$$r_Y = \frac{(\beta \pi)^{-1}(n-1)}{(n+1)} \left(\frac{K}{\sigma_{YS}} \right)^2 \quad (27)$$

$$\phi = \frac{1}{1 + \left(\frac{P'}{P_{00}} \right)^2} \quad (28)$$

$$P_{00} = 1.455 * \eta * b * \sigma_{YS} \quad (29)$$

$\beta = 6$ for plane strain and 2 for plane stress [Ref. 28]

b =uncracked CT specimen ligament (see Figure 15)

$$\eta = \sqrt{(2a/b)^2 + 2(2a/b) + 2} - (2a/b + 1) \quad [\text{Ref. 28}] \quad (30)$$

K =stress intensity factor

The stress intensity factor formula outlined in ASTM E399 was utilized.

where;

$$K = \frac{P}{Bw^{1/2}} f(a/w) \quad (31)$$

$$f(a/w) = \frac{(2 \cdot a/w)(0.886 + 4.64a/w - 13.32(a/w)^2 + 14.72(a/w)^3 - 5.6(a/w)^4)}{(1 - a/w)^{1.5}} \quad (32)$$

h_1 , h_2 and h_3 are listed in reference [Ref. 28] in tabular form.

A program was written in Matlab 4.0, produced by Mathworks, which calculates all of the above parameters as a function of varying load (P) and crack length (a), and various material properties and geometrical parameters. The user must input the following terms into the program

- 1) all values of (V_g P) from the experimentally determined Load (P) vs. clip gage displacement plot.
- 2) n , α , E , initial unloading compliance, σ_{ys} , a_0 , w , V and B , a_{max} and interval of a .

The program then calculates all possibilities of J , V_g and V_{II} for the above properties and geometrical parameters for each value of experimental P , within a pre-determined range of a (0 - a_{max}). Next, it performs a comparison of experimental V_g and numerical V_g where the corresponding J and a values are determined.

It should be noted that the Equations for $F1$, $V1$ and $V2$ are only valid for $0.3 < a_E/w < 0.7$. Consequently, for a_E/w values outside of 0.7 , the final value of $F1$, $V1$ and $V2$ at $a_E/W=0.7$ is used when $a_E/w > 0.7$. These parameters are used solely for the elastic contribution of J . Accordingly, at this point, the material will be experiencing severe plastic deformation which should govern the magnitude of J whereby computed values of J will be lower than expected due to this approximation. Thus, conservative estimates of J are obtained. Moreover, the elastic contribution at $a_E/w=0.7$, as long as $a_0/w < 0.7$, will be small and rising slowly in comparison to the plastic contribution. However, it is anticipated that enough J vs. a points will have been obtained, within the exclusion zone, to establish the JR curve's shape and comply with ASTM 813-89 and ultimately determine J_{Ic} , before this limitation is reached.

IV. RESULTS AND DISCUSSION

A. PRIOR MICROSTRUCTURAL FINDINGS

Dutta [21,31] concluded that PSN did occur in material numbers 13185 and 13184 following extrusion, but not in 13186. It was observed through TEM analysis [Ref. 31], that the material which underwent higher strain rates (13185 and 13184) possessed significantly finer grain sizes (2-4 μm relative to 6-8 μm for 13186), suggesting the occurrence of PSN.

TEM analysis revealed resolvable dislocations near the grain/sub-grain boundaries of the higher temp extrusion (13184), thus concluding that some of the boundaries are low angle. Even though no dislocations were resolved in the lower temperature extrusion of the same strain rate (13185), electron diffraction studies revealed that while most grain boundaries in the material that underwent PSN (13185) were high angle in character, some grains boundaries possessed misorientation angles of the order of 5-7 $^{\circ}$ only [Ref. 31]. Thus, even after complete recrystallization via PSN, a combination of high and low angle boundaries is produced. Conventional recrystallization under non-PSN conditions (13186), on the other hand, revealed only high angle grain boundaries.

Another interesting feature that was observed by Dutta [Ref. 31] was that many of the recrystallized grains which nucleate at the SiCp-matrix interface were stabilized by finer (sub-micron) SiCp, which were present in the composite along with the larger reinforcements. Thus, the bi-modal distribution of SiCp in the present composite helped keep the grain size fine by pinning, and thereby stabilizing the mobile grain boundaries following recrystallization.

B. MICROSTRUCTURAL FINDINGS RESULTING FROM THE NOTCHED TENSILE SAMPLES

Figures 19 and 20 show the region ahead of the unfailed notch in the double notched tensile samples following sectioning and metallographic polishing. Relatively little information

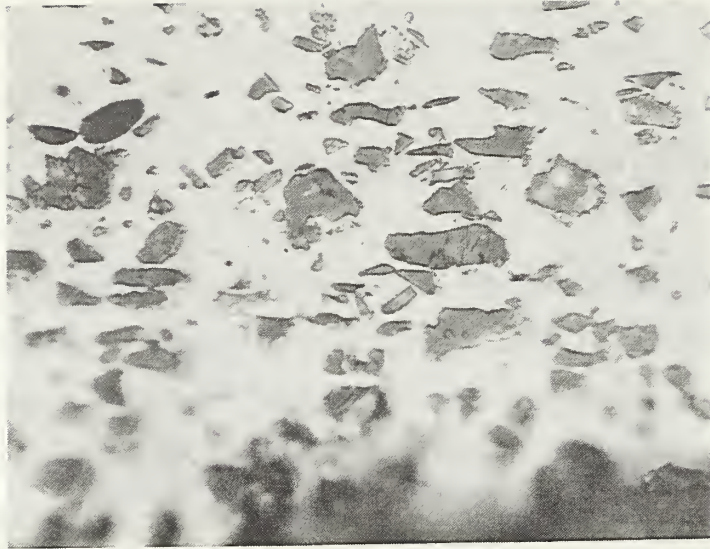


Figure 19: Optical photograph revealing cracked particles near the notch for matrix in T6 condition. Loading axis is horizontal. 1000X.

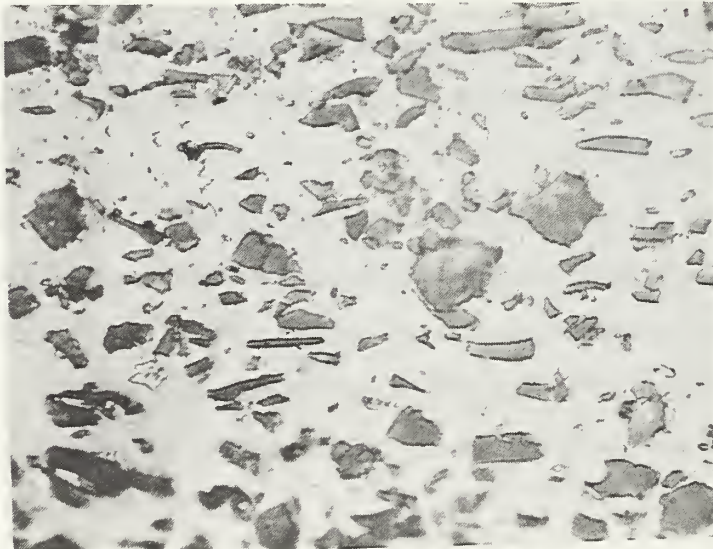


Figure 20: Optical photograph revealing few cracked particles near the notch for matrix in SA condition. Loading axis is horizontal. 1000X.

as to the modes of cracking is observable in either sample. Figure 19 (of T6 sample) reveals some particle cracking perpendicular to the loading direction in the vicinity of the unfailed notch. Figure 20 (450°C) reveals less cracked particles perpendicular to the loading direction.

Figures 21 and 22 show SEM photographs of the fracture surfaces of the composite in the -T6 and -450 conditions, respectively. Figure 21 (of T6) clearly demonstrates flat faceted (i.e., cleaved/fractured) particles. The matrix reveals relatively little ductility, and shows very shallow dimples. Figure 22 (450°C) tells a different story. The obvious difference is less particles on the failure plane and the presence of deeper dimples. Absence of SiCp on the surface strongly indicates failure through the matrix, with possibly some failure along the reinforcement-matrix interface. Additionally, the deeper dimples present in the 450°C static annealed (SA) matrix is indicative of significant pre-failure ductility along with high fracture toughness. Figures 23-26 are optical micrographs which provide an overall picture concerning the distribution of particles in the vicinity of the notch and far removed from the failure.

Similar results have been found earlier [Ref. 21] based on microscopic examination of the region near the crack tip in sectioned compact tension specimens subjected to loading. Whereas significant particle fracture was noticed ahead of the crack front in the DRA treated to -T6 condition (Figure 19), relatively little particle failure was observed in the sample annealed at 450°C (Figure 20). The following rationale can be offered for these observations. The matrix in the 450°C sample is very soft, and hence, matrix failure occurs before the particles can be loaded up enough to cause particle fracture. On the other hand, the matrix in the -T6 sample is significantly stronger, and the stress intensity ahead of the crack tip can rise to a level adequate to cause fracture of particles at and some distance away from the crack tip, even though the matrix in the immediate vicinity of the crack tip remains unfailed (because of its higher toughness than the SiCp). Once particle cracking occurs ahead of the crack front, failure occurs rapidly by linkage of the cracks through the matrix.

Based on the above, it is clear that in order to optimize the fracture toughness - strength relationship in DRA, the preferred approach would be to produce a matrix condition which is strong enough such that matrix failure does not occur prematurely (i.e., prior to adequate loading of the particles to produce the desired composite strength level), but soft enough such that

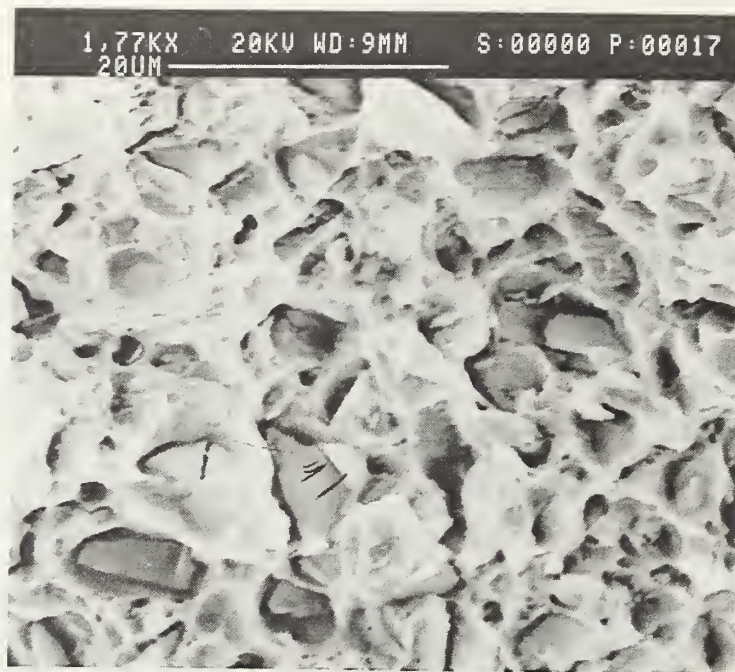


Figure 21: SEM micrograph for fracture surface of matrix in T6 condition. Notice numerous faceted and cracked particles. One particle near center lower edge reveals a scratch resulting from photo processing, not a crack. 1770X.

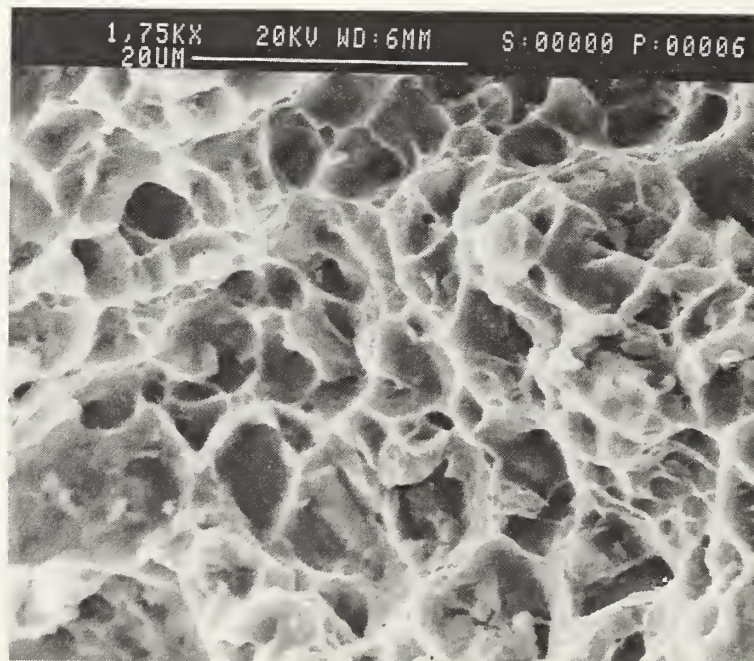


Figure 22: SEM micrograph revealing no SiC particles on fracture surface of matrix in 450°C SA. Surface indicates failure through matrix vs. particles. 1750X.

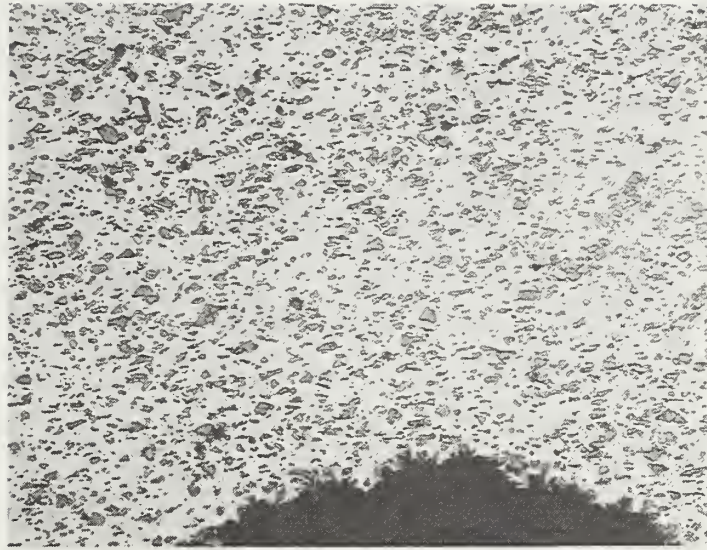


Figure 23: Optical micrograph near notch for T6 matrix. 200X.

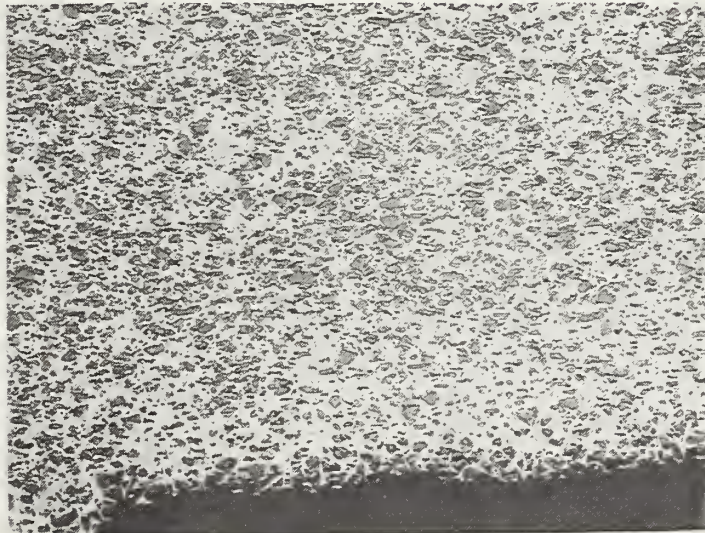


Figure 24: Optical micrograph near notch for matrix in 450°C SA. 200X.



Figure 25: T6 matrix far removed from failure. 320X.

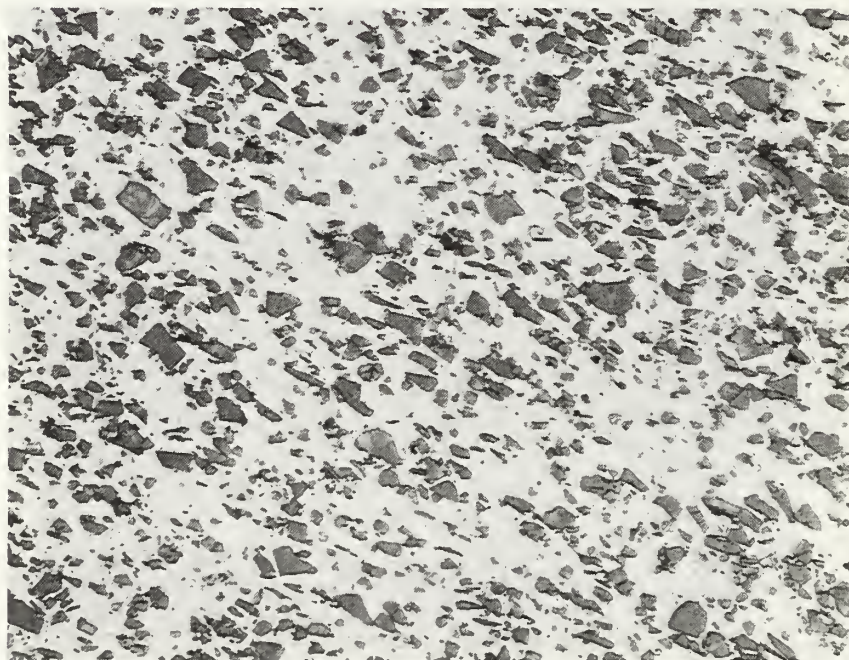


Figure 26: 450°C SA matrix far removed from failure. 320X

eventual failure is matrix controlled, rather than particle controlled. Therefore, the approach taken in this research consisted of producing a number of matrix strength levels which are intermediate between those of the -T6 and 450°C SA conditions.

C. MECHANICAL PROPERTIES

Table II summarizes the mechanical properties of the three extrusions under various heat treatment conditions.

Figure 27 [Ref. 21] shows the impact of processing and heat treatment on the fracture toughness-strength relationship in the SiCp-6092 Al composite. A number of points are evident. First, with increasing process strain (3.58 to 5.83), the strength toughness combination improves because of improved homogeneity in reinforcement distribution. A significant further improvement is obtained due to matrix grain refinement via PSN at a constant process strain of 5.83. Static annealing at 450°C followed by water quenching decreases the yield strength substantially, but results in a very large increase in fracture toughness, changing the crack propagation mode from unstable to stable. Thus this heat treatment offers the potential of enhancing fracture toughness without underaging the matrix, which is not desirable since it produces an unstable microstructure which ages with time. Further, complete solution treatment, in any case, is unable to offer the high toughness (and the commensurately low strength level needed to achieve this) produced by the 450°C SA condition (see data for 6061 Al -15 vol.% Al₂O₃ in Figure 27).

In the present work, the focus was to produce a range of conditions intermediate between the strong, relatively brittle -T6 condition and the soft but tough 450°C condition.

Figures 28-30 show the K_{eq} vs yield strength data for samples numbers 13184, 13185 and 13186, respectively, in various heat treatment conditions. The concept of an equivalent fracture toughness (K_{eq}) was used since some of the samples showed stable crack propagation and displayed a JR curve, whereas some others failed catastrophically, but did not satisfy the

Table II: Summary of Mechanical Properties: DVA 6092 Al - 17.5%v/o SiCp MMC

Material	E (GPa)	YS (MPa)	UTS (MPa)	%Elong	K _{eq} (MPa*m ^{0.5})	J _{IC} (kJ/m ²)	Tearing Modulus
As received-T6	75	356	398	2	18		
13184-450	102	150	270		36.693	11.851*	37.344
13185-450	102	160	270	12.6	38.87	13.3*	31
13186-450	102	150	270	12.5	36.162	11.511*	29.006
13185-450-170	110	270	293.5	14.18	31.246	7.968*	15.255
13186-450-170	96.4	260	293	16.7	33.058	10.178*	12.174
13184-480-170	115	300	447	7.15	25.68		
13185-480-170	115	300	451	7.5	26.722		
13186-480-170	112	275	331.4	11.53	29.263	6.715*	18.02
13184-T4 (9 Mo)	107	345	483	6.7	27.983		
13185-T4 (9 Mo)	106	345	481.9	6.25	28.424		
13186-T4 (9 Mo)	104	345	482	6.9	28.194		
13184-T6	131	450	490	2.8	26*		
13185-T6	135	455	503	4.3	27*		
13186-T6	102	430	488	3.6	23*		
13185-560-450	105	225	319	16	31.958	8.733*	27.275
13185-560-450-170	105	310	321	12.2	29.684		
Al 6061 - T6	75	270	325	12	29*		

*= values which satisfied plane strain conditions

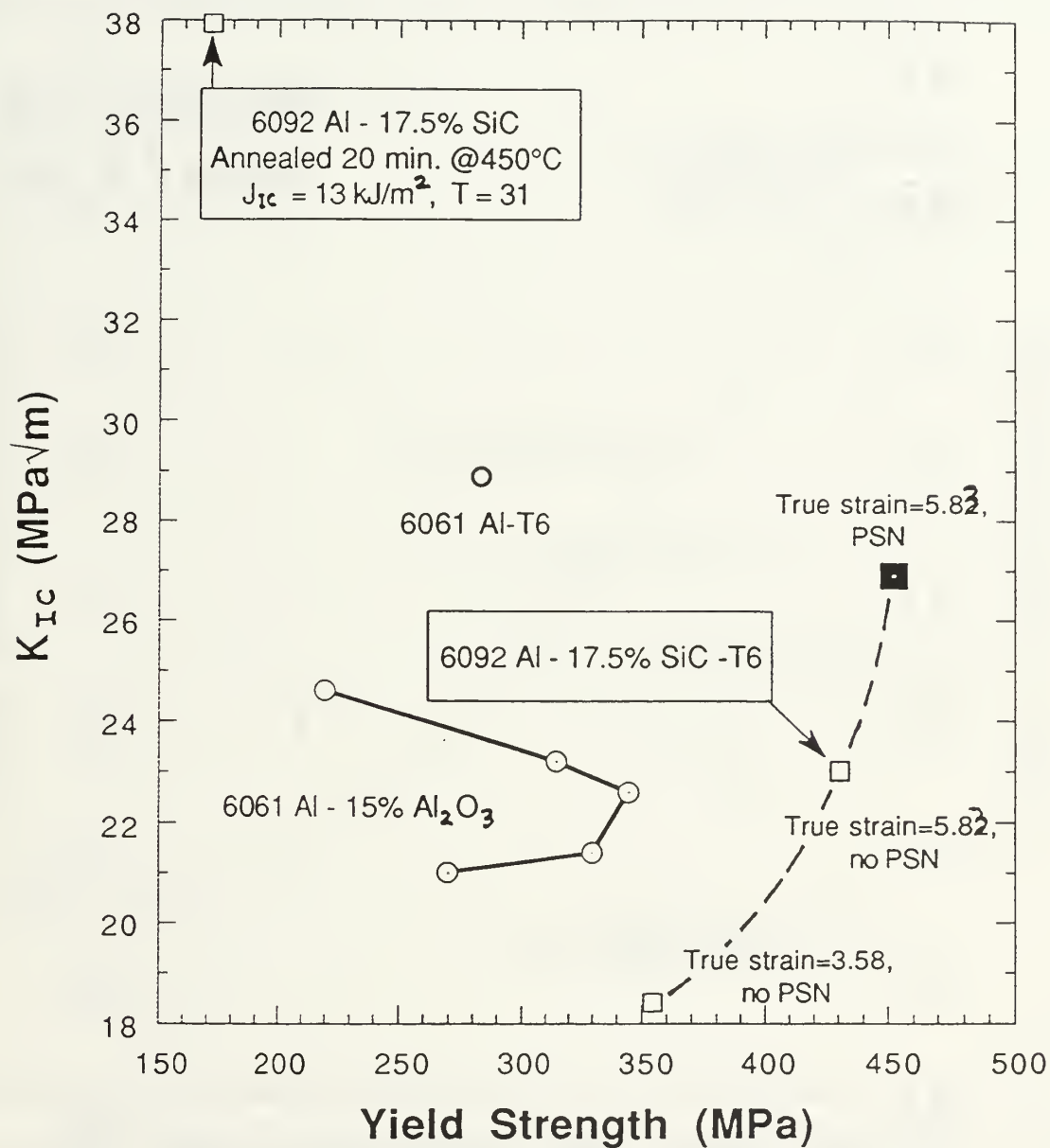


Figure 27: Effect of Processing on 6092 Al-17.5% SiCp. From Reference [21].

13184 Keq vs. Yield Strength

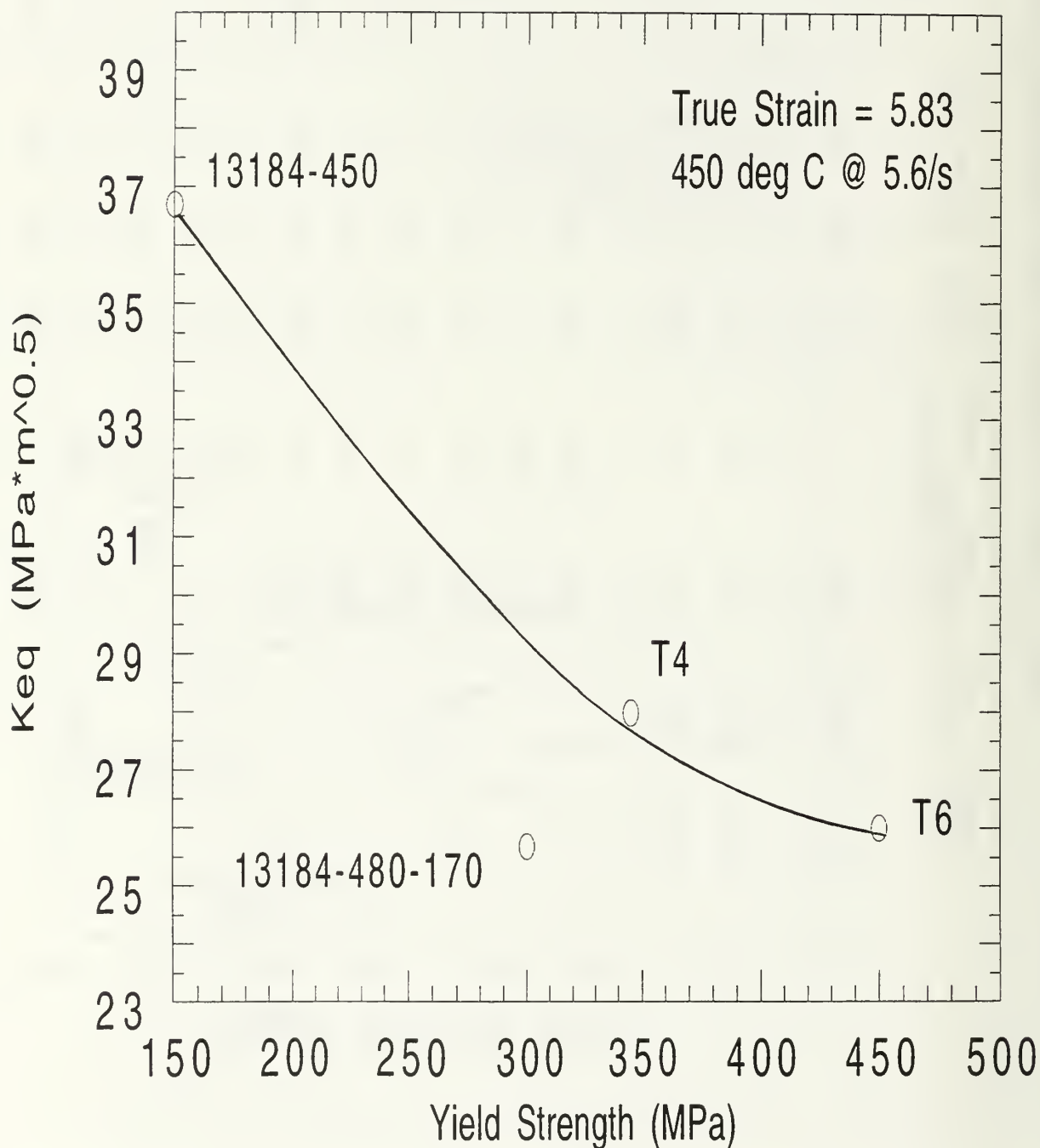


Figure 28: 13184 Keq vs. Yield Strength

13185 Keq vs. Yield Strength

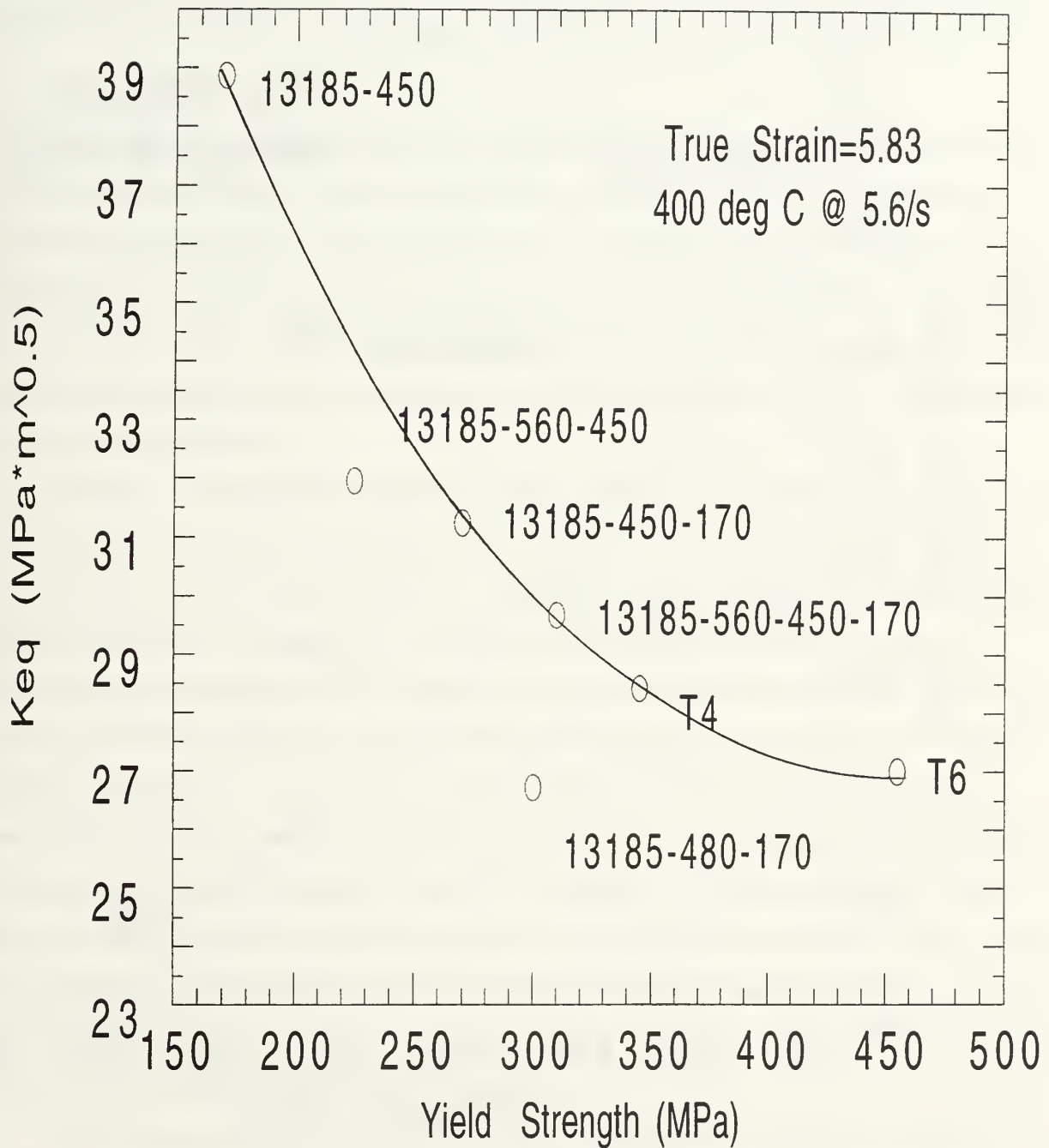


Figure 29: 13185 Keq vs. Yield Strength

13186 Keq vs. Yield Strength

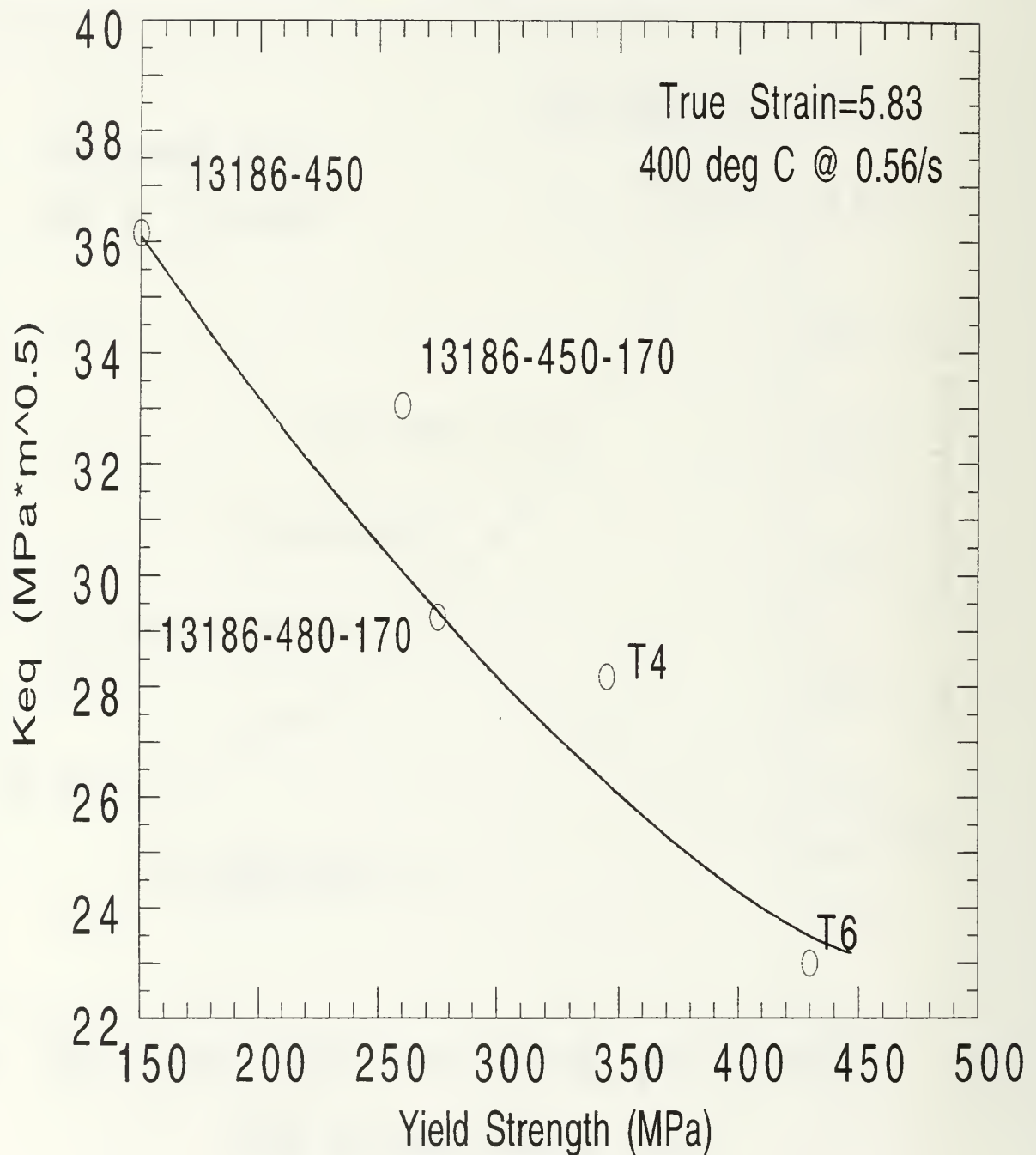


Figure 30: 13186 Keq vs. Yield Strength

plane strain condition. In Table II, K_{eq} data from tests which did satisfy the plane strain condition are marked with an asterisk. All JQ values satisfied the conditions for J_{Ic} and were converted to K_{eq} by the following relation:

$$K_{eq} = (J_{Ic} * E / (1 - \nu^2))^{1/2} \quad (33)$$

As noted earlier, the extremes in each Figure (Figures 28-30) are represented by the soft, tough 450°C SA condition, and the strong, relatively brittle -T6 condition. Most of the other heat treatments are observed to produce a range of conditions intermediate between these extremes, and fall roughly on one curve. However, for each sample, the -480-170 condition (representing a solution anneal at 480°C followed by artificial aging at 170°C) lies well below this curve. This suggests that the microstructure produced during the solution treatment at 480°C is detrimental to the mechanical properties.

Figure 31 shows a plot of the data for 13184, 13185 and 13186, superimposed on one graph. Some general trends emerge from the combined data. The data for all the three sample sets are observed to show similar trends, as noted earlier. However, appreciable differences in the slopes of the K_{eq} vs σ_{YS} data for the three samples are apparent. It is clear that in general, the PSN condition (represented by 13185) offers the best fracture toughness - strength combination at the low and high strength levels. At the intermediate strength levels, however, this advantage is reduced significantly. In general, the non-PSN condition (represented by 13186) offers the worst fracture toughness strength combination at all strength levels, although the disadvantage is minimal in the intermediate strength levels (250 - 350 MPa). 13184, which did show PSN of recrystallization, but produced grain boundaries with relatively low misorientation [Ref. 31] and was processed near the boundary of the PSN and the non-PSN regimes, appears to have properties similar to those of the PSN condition at the higher strength level, but similar to those of the non-PSN condition at the lower strength levels.

Thus it can be inferred that complete PSN of recrystallization, resulting in a fine matrix grain size with highly misoriented grain boundaries, yields the best properties, with the advantage over the non-PSN state being more pronounced at the low and high strength ends, but

Keq vs. Yield Strength

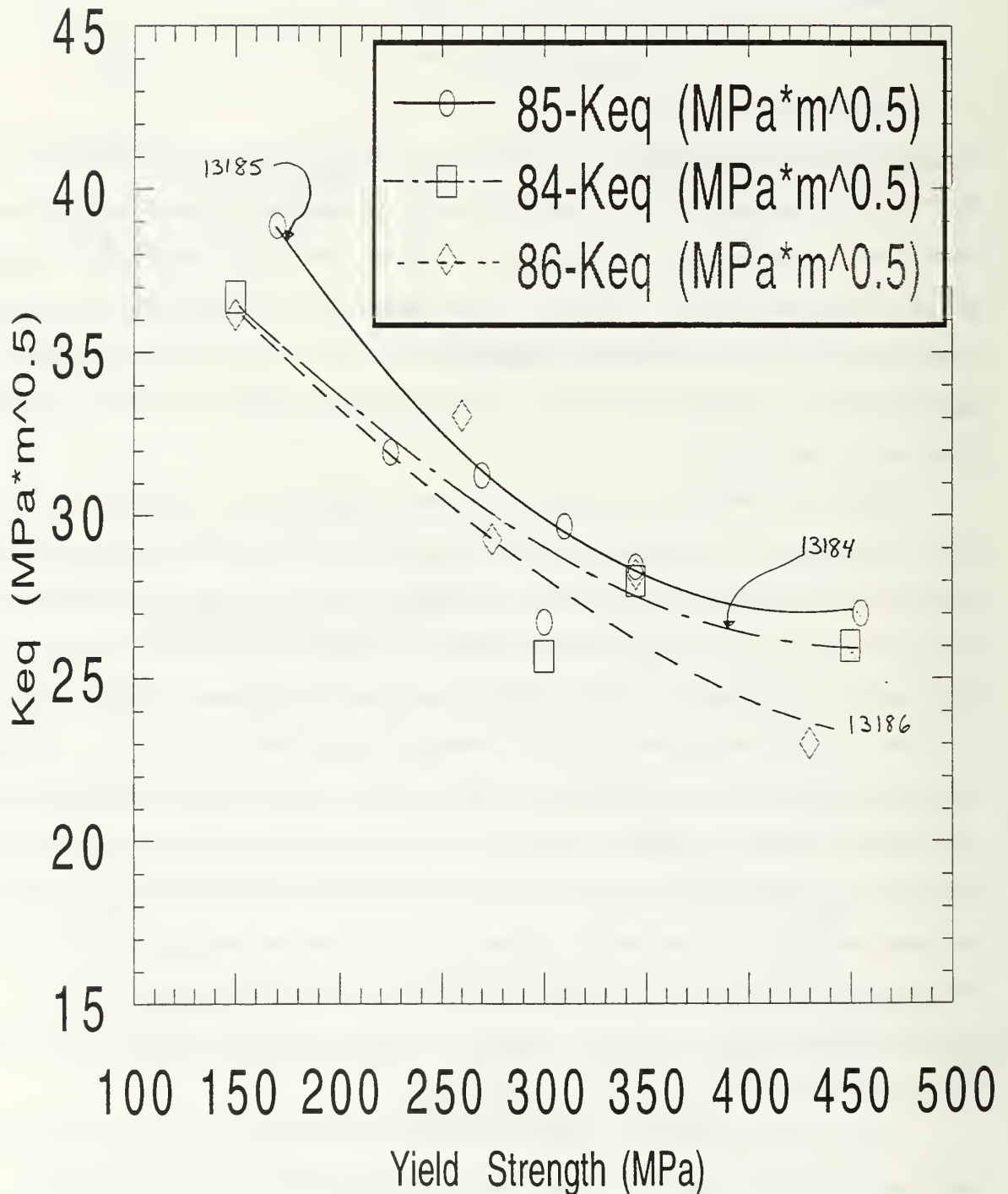


Figure 31: Combined Keq vs. Yield Strength for 13184 thru 13186. Notice trends where material which underwent PSN (13185) lies above those which did not recrystallize (13186). All values were obtained from Table II.

less so in the intermediate strength range. Under process conditions at the boundary between PSN and non-PSN conditions, where PSN occurs, but produces grain boundaries with low misorientations, fracture properties are better at the high strength end (-T6 condition) relative to the non-PSN condition, but the advantage ceases to exist at lower strength levels. Further work is necessary to determine the rationale for these trends in mechanical properties based on a mechanistic standpoint.

Figure 32 shows the K_{eq} vs. % elongation to failure data for all the samples in one combined plot. In general, it is apparent that as fracture toughness of the materials increases, so does the % elongation. This is expected, since soft, ductile matrices usually possess high crack initiation toughnesses. Most of the data in Figure 32 lie within one linear (albeit broad) band, showing a direct correlation between K_{eq} and tensile ductility. However, some exceptions are to be noted. First, the data for the samples solution annealed at 450°C lie well outside this broad but linear band. Both the crack initiation and propagation toughnesses of these samples are significantly greater than what would be expected based on the tensile ductilities of these samples.

Additionally, the samples solution annealed at 480°C lie near the lower edges of the band, suggesting that this heat treatment yields a lower fracture toughness than would be expected based on its tensile ductility. This may be attributable to the large incoherent precipitates present in the matrix in this condition, as noted in section 4 of the Results and Discussion section.

Further, it is noted that although PSN provides a considerable increase in K_{eq} , the corresponding gain in tensile ductility due to the grain refinement is relatively small.

Figures 33-35 show some representative load versus clip gage displacement plots for fracture via unstable and stable crack propagation. Notice that all treatments which possessed an aged (artificial or natural) matrix failed catastrophically, with unstable crack propagation. Conversely, the treatments which ended with a solution anneal or a full solutionization displayed stable crack propagation with ductile load vs. clip gage displacement (V_g plots. Additionally, although the ductile failure modes are similar, 13185-450 (Figure 34) appears to absorb more

Keq vs. % Elongation

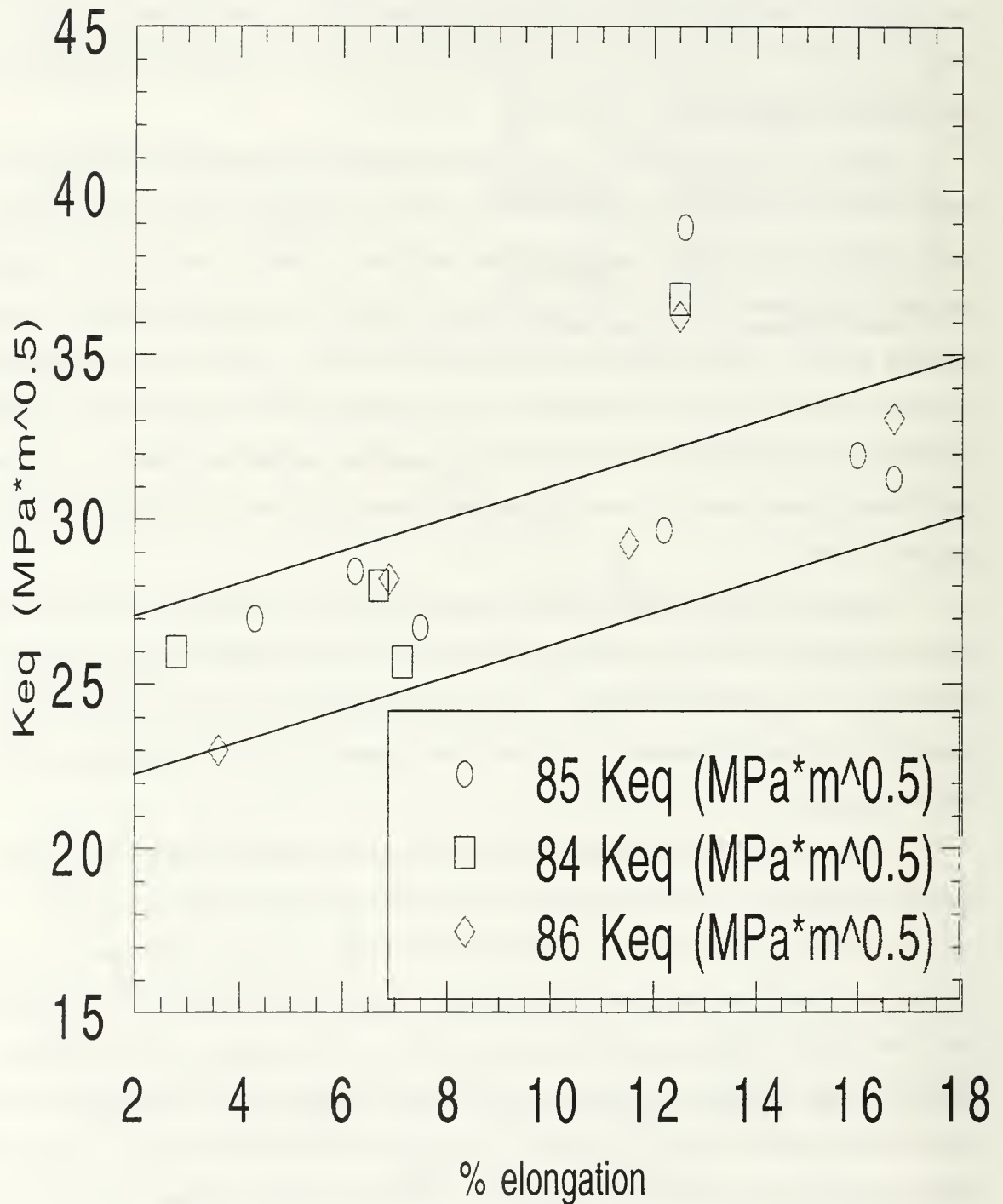


Figure 32: Combined Keq vs. % elongation for 13184 thru 13186. Notice all but SA treatments lie on a linear broad band which represents a correlation between ductility and Keq. All values were obtained from Table II.

AS-RECEIVED T6

LOAD VS. CLIP GAGE DISPLACEMENT

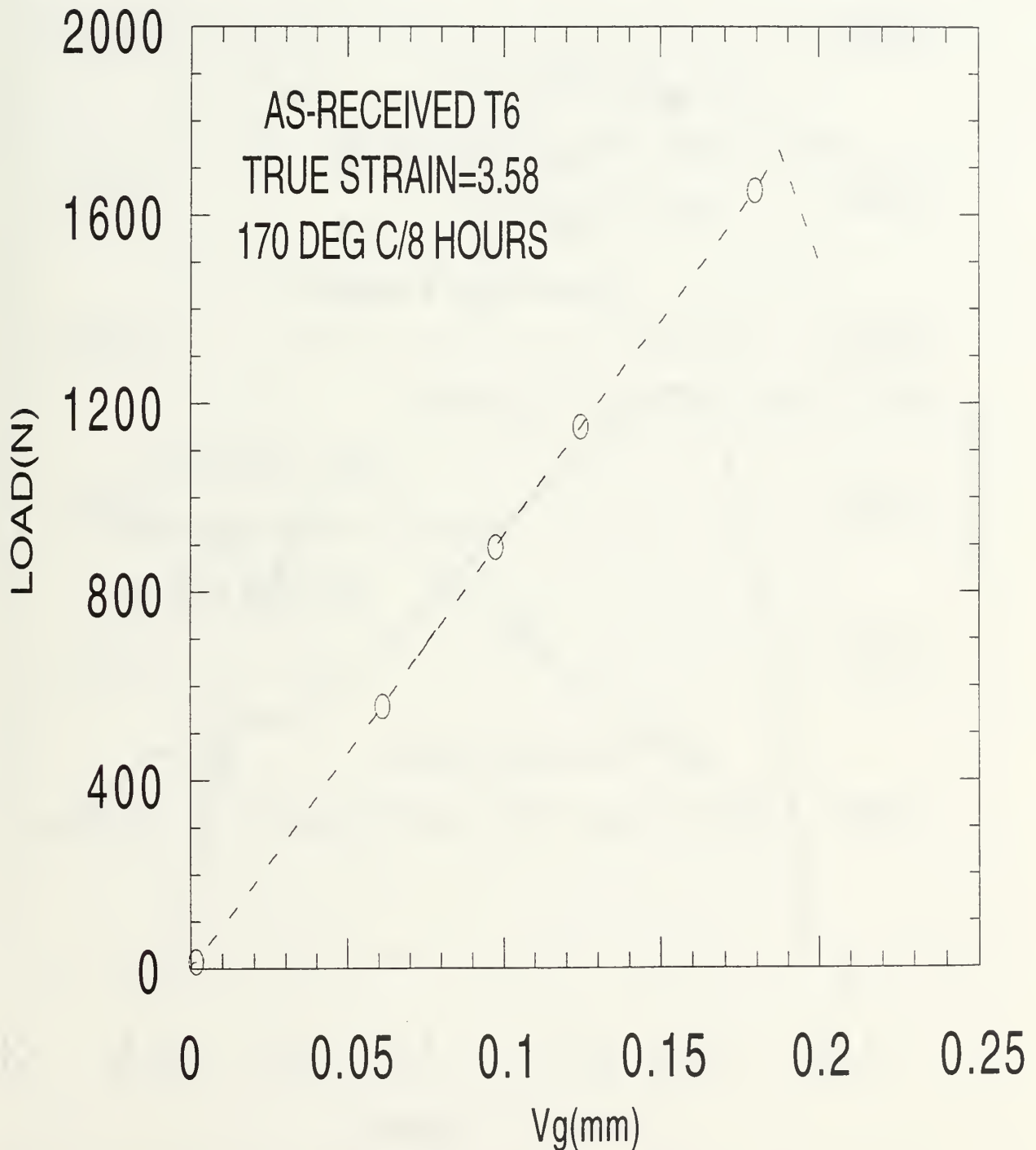


Figure 33: As-Received 6092 Al 17.5 vol% SiCp in T6. True Strain=3.58, experimental load vs. clip gage displacement.

LOAD VS. CLIP GAGE DISPLACEMENT

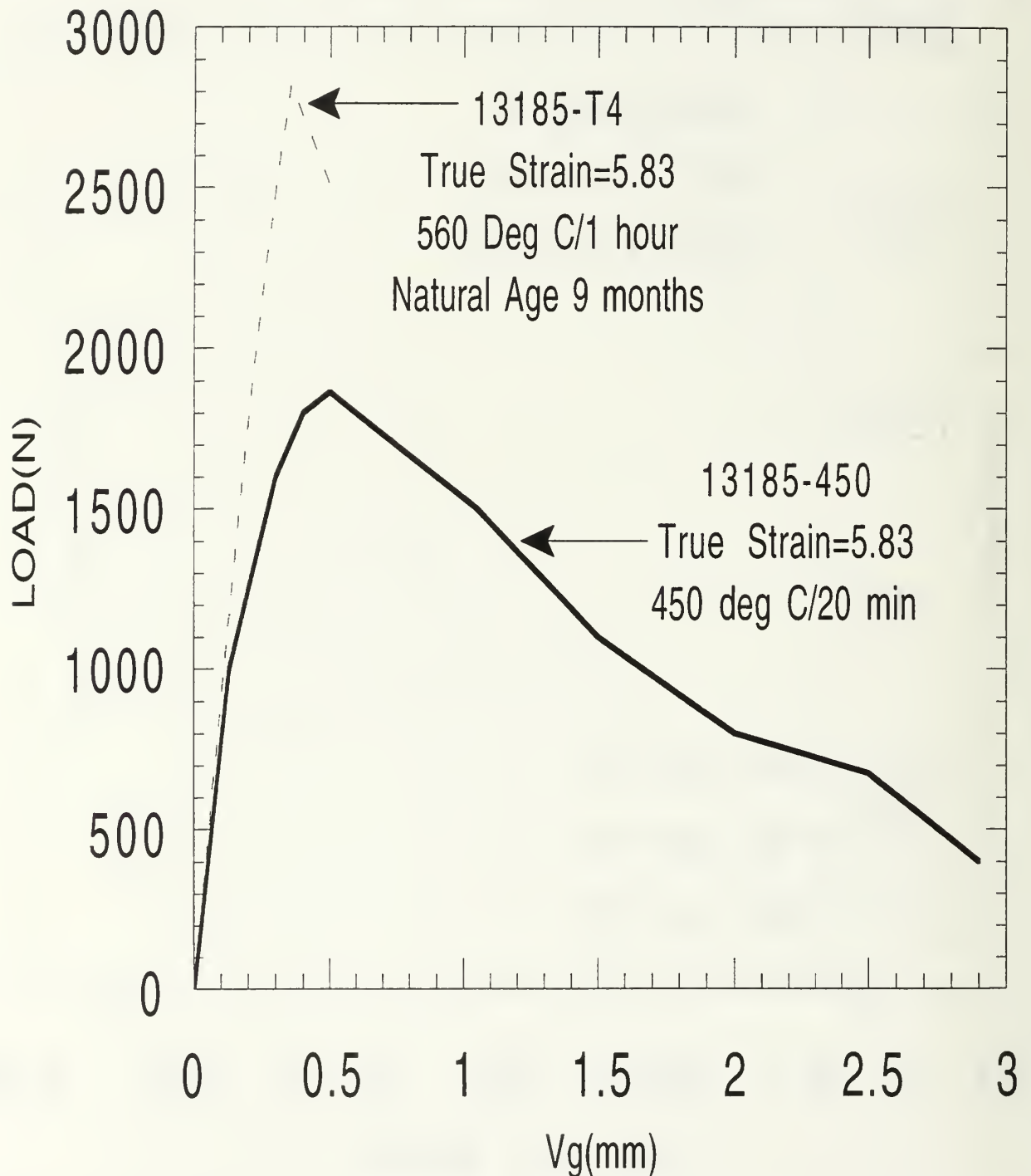


Figure 34: 13185-T4, 13185-450 experimental load vs. clip gage displacement

LOAD VS. CLIP GAGE DISPLACEMENT

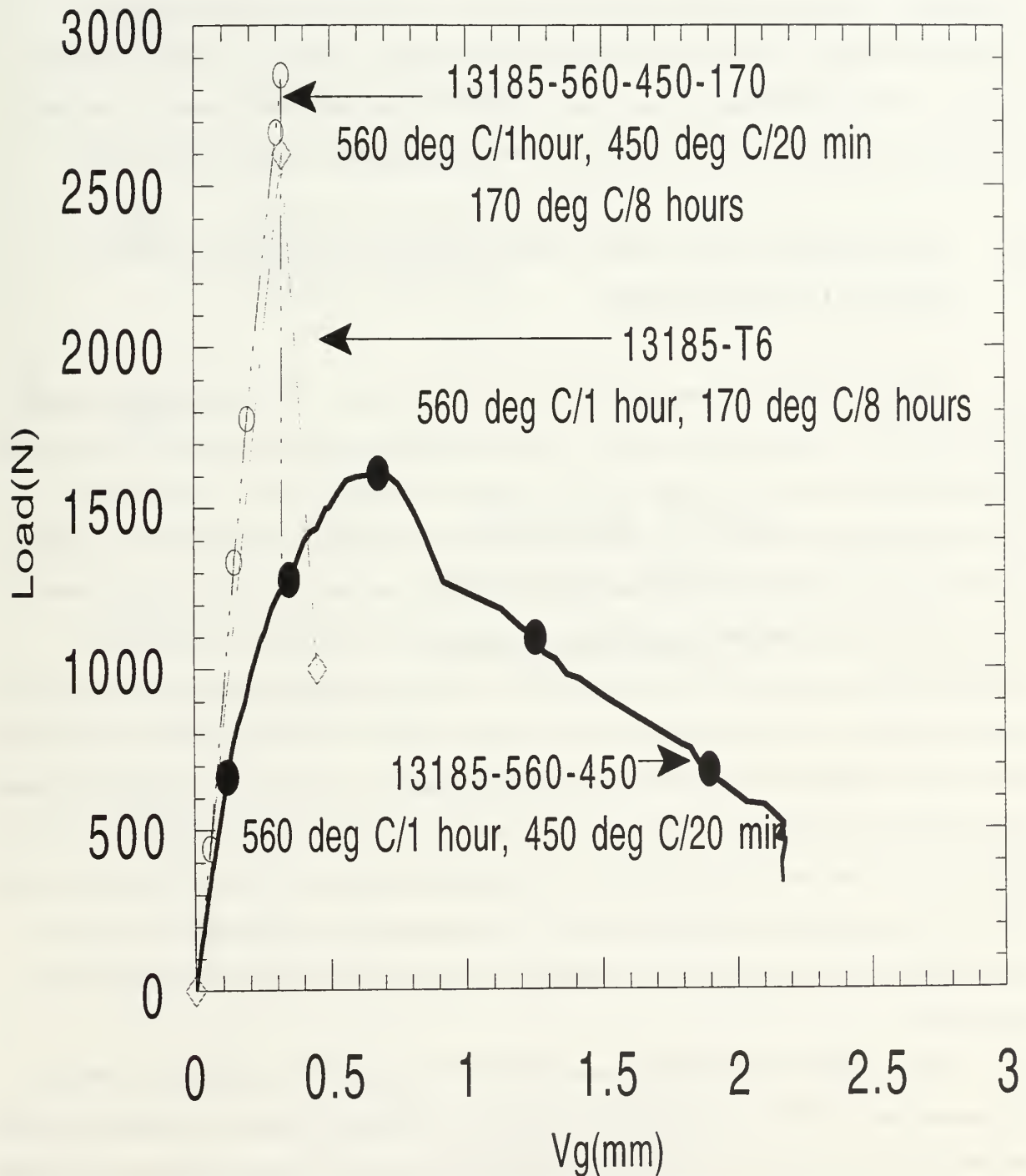


Figure 35: 13185-560-450-170, 13185-T6, 13185-560-450 experimental load vs. clip gage displacement.

energy in comparison to 13185-560-450 (Figure 35). This is reflected in the higher K_{eq} data for 13185-450 relative to 13185-560-450 (Table II, Figure 29).

Figures 36-37 show the J-resistance curves for 13185-560-450 and 13185-450 respectively. Of note are the very high slopes of the J vs Δa plots for both samples, indicating that both samples have very high crack propagation resistances (tearing modulus). However, 13185-450 (Figure 37) possesses a higher crack propagation resistance, as well as a higher crack initiation resistance (as indicated by J_{Ic}), and therefore has the greater K_{eq} .

D. MICROSTRUCTURAL EVOLUTION DURING PROCESSING AND IT'S IMPACT ON PROPERTIES

While the 13185-450 sample offers the greatest toughness, the corresponding strength level of 170 MPa is too low for the DRA to be of practical use. Figure 38 [Ref. 21] shows DSC scans of the test composite (13186) in the fully solution treated (at 560°C) condition, after solution annealing at 450°C (-450), and after solution annealing at 450°C followed by aging at 170°C for 8 hours (-450-170). It is clear that after solution annealing at 450°C the volume of transition precipitates that can be produced in the matrix during subsequent annealing is significantly less than after full solution treatment. However, an appreciable amount of solutes are still dissolved in the matrix after the 450°C anneal, which can be precipitated out in the form of β'' and β' , offering the possibility of increasing the hardness of the 13185-450 state by further heat treatment. Figure 38 also shows a DSC scan of the 13185-450 sample following a 170°C 8 hour age. It is observed that nearly all the β'' is now precipitated out, with only a small quantity of β' left to be precipitated after this treatment. Commensurately, the strength level of the composite after this heat treatment is significantly higher than that of the -450 state (Table II, Figure 29)

Figure 39 shows DSC thermograms of the PSN and non-PSN samples, after complete solutionization at 560°C (13185-560 and 13186-560). Although the basic precipitation processes are very similar, the precise details of the precipitation behavior of the two samples with different process histories are quite different. It is apparent that the GPI zones are relatively less in volume

13185-560-450

J Resistance Curve

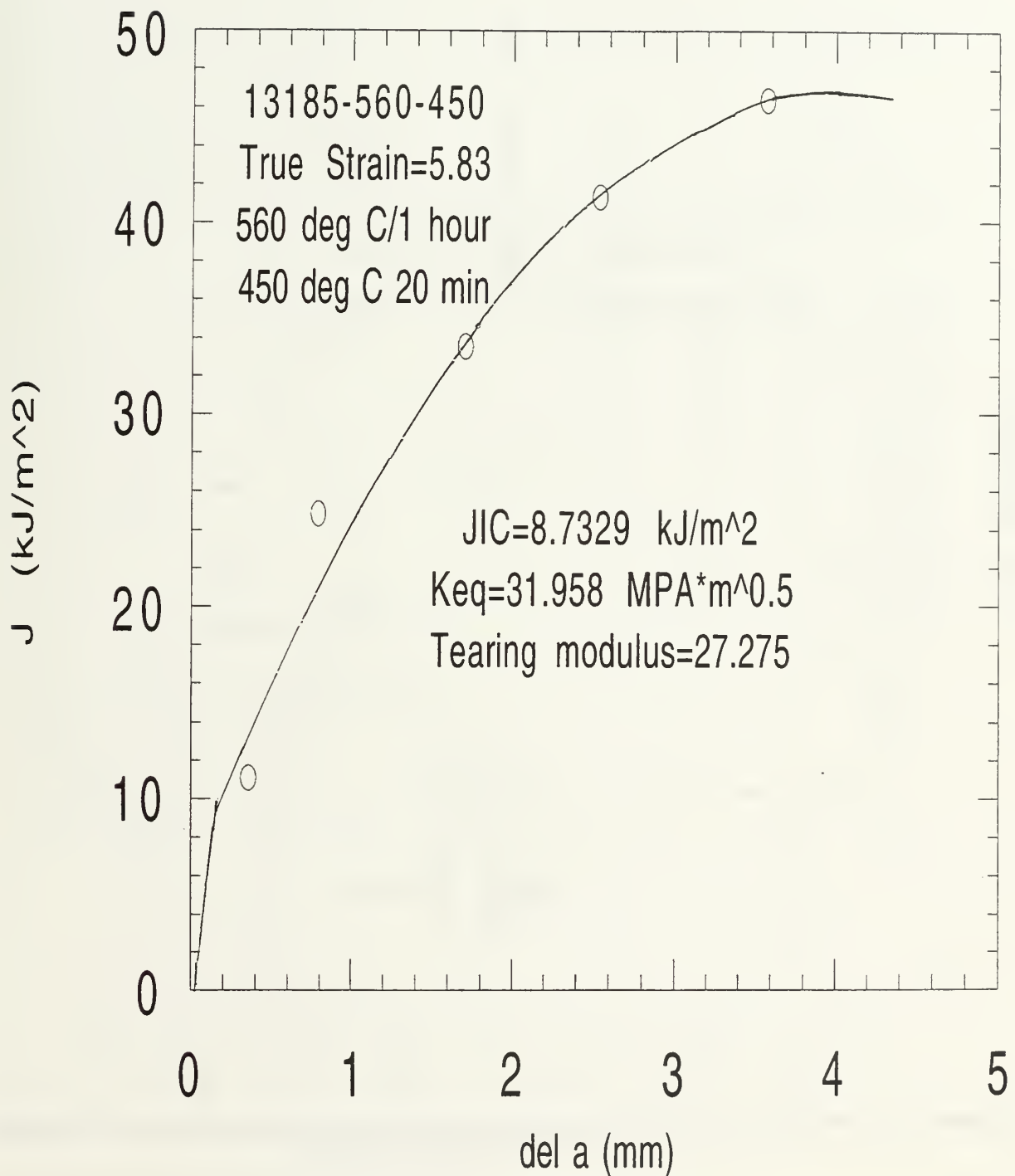


Figure 36: JR curve for 13185-560-450. Notice steep blunting lines representing high crack propagation resistance.

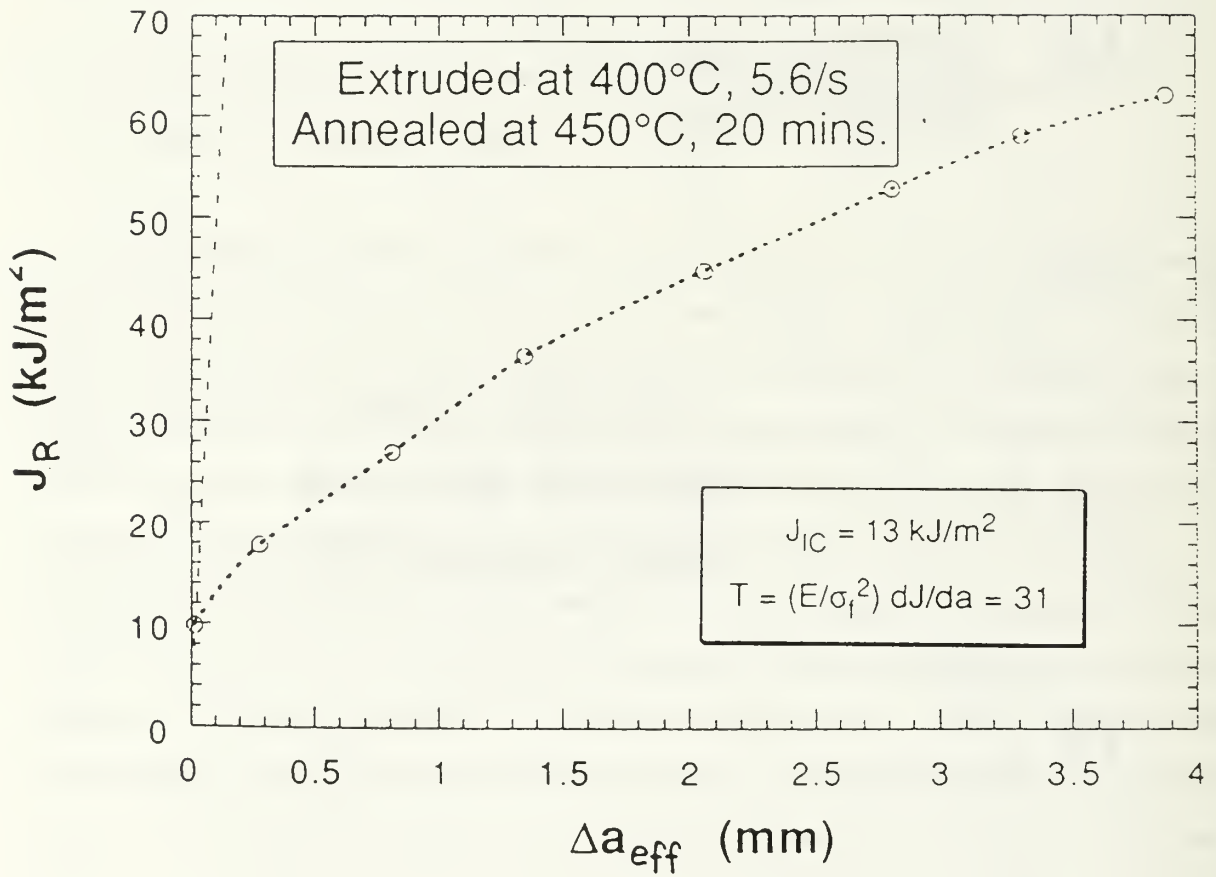


Figure 37: JR curve for 13185-450. Notice steep blunting lines revealing high crack resistance.

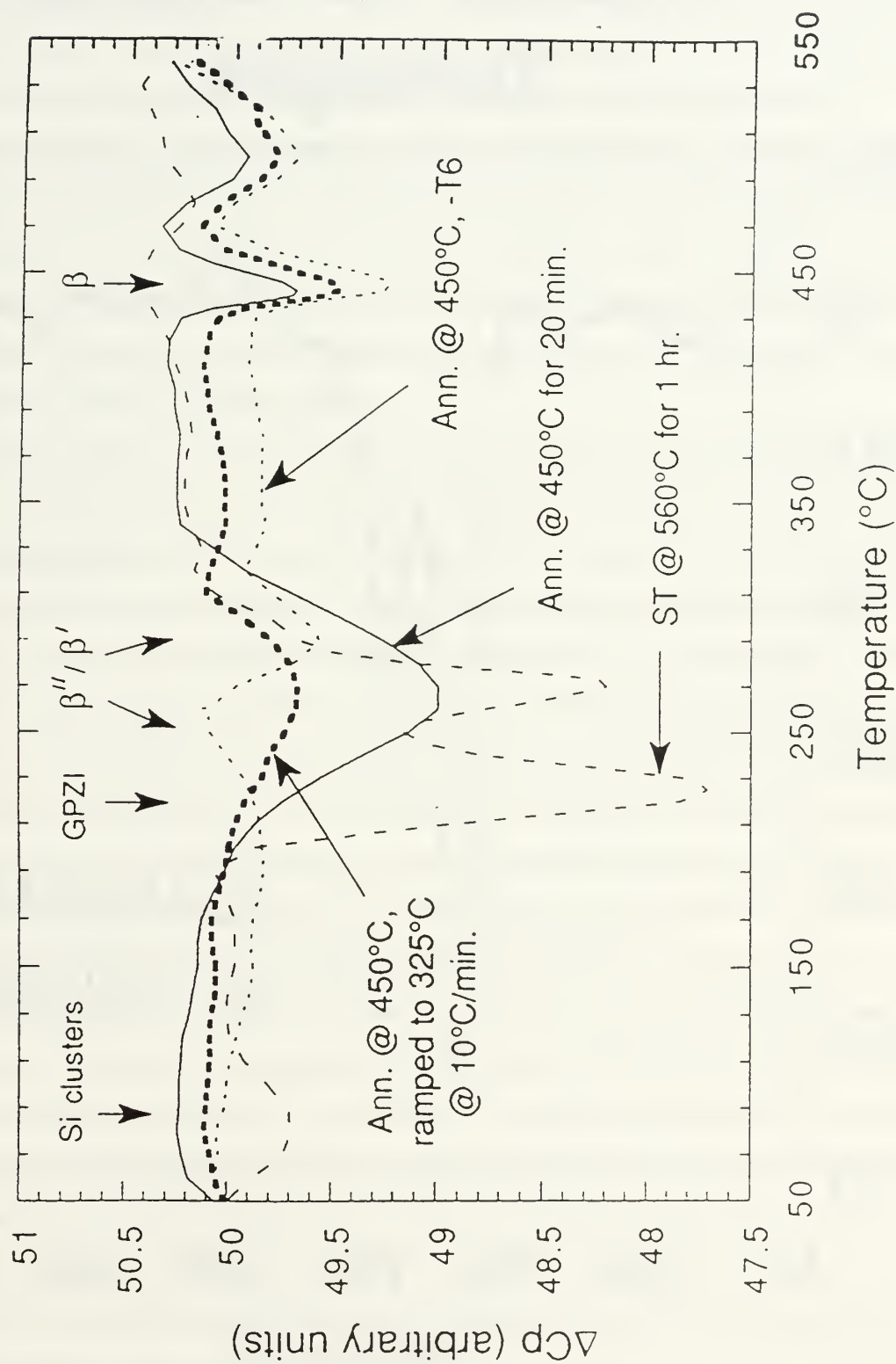


Figure 38: 13186 DSC thermogram representing the potential for strengthening following a 450°C SA.

13185-560 vs. 13186-560 Thermogram

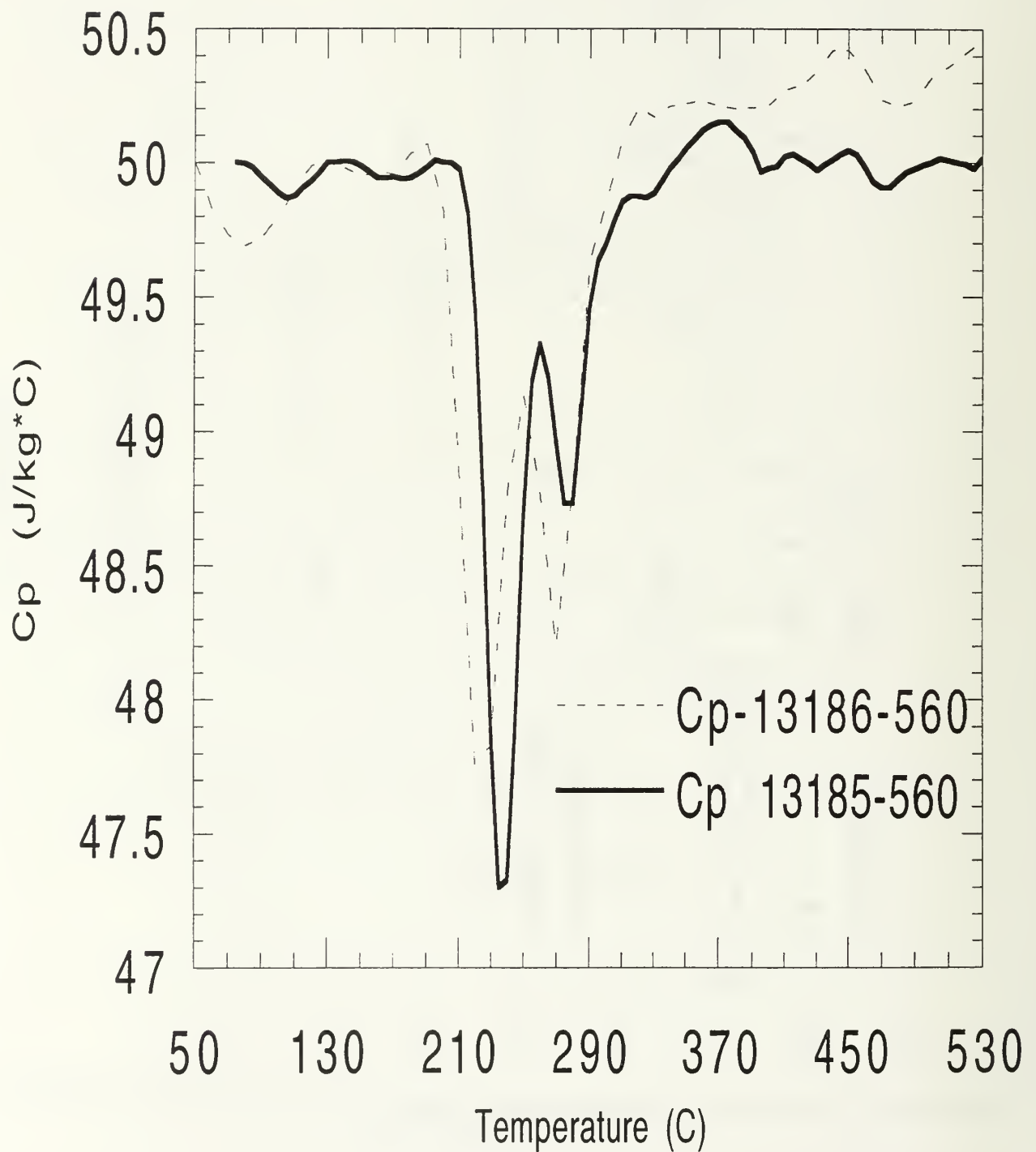


Figure 39: DSC Thermogram for 13185-560 and 13186-560.

fraction in the 13185-560, whereas the amounts of the GPII zones and β' in 13185-560 are more. Since GPII and β' are the primary hardening precipitates in 6XXX Al alloys, 13185 is expected to achieve greater strength levels than 13186 in the aged condition, possibly with a commensurate price in terms of toughness, although this price is likely to be reduced due to the finer matrix grain size in 13185. Additionally, all precipitation processes appear to be somewhat accelerated in 13185-560 relative to 13186-560. Therefore, in order to optimize the fracture toughness-strength relationships in these DRA materials, it is important to carefully consider the precise processing history and its influence on precipitation prior to determining the heat treatment to achieve the desired results.

Figure 40 shows the DSC thermograms for the composites processed in the PSN and non-PSN regimes after a solution anneal at 450°C (13185-450 and 13186-450). It is apparent that following identical heat treatments, the amount of precipitates that can be obtained in the two composites are quite different. From the shape of the peak, which represents a β'' / β' doublet, it is apparent that significantly less β'' is available for precipitation in the 13185 (PSN) material. This is suggestive of the possibility that 13185-450 is in an advanced state of aging relative to 13186-450, possibly accounting for part of its 10 MPa yield strength advantage over 13185-450. Despite this higher yield strength, of course, 13185-450 possesses a higher K_{eq} (Table II) because of its finer matrix grain size. Following artificial aging at 170°C it can be seen from Table II that the K_{eq} for 13185-450 drops more sharply (38.87 to 31.25 MPa) than that for 13186-450 (36.16 to 33.06 MPa), with no commensurate strength advantage. A close inspection of Figure 40 suggests a possible reason. The hardening of 13185-450 during artificial aging occurs mainly due to β' precipitation, with relatively little β'' precipitation. Conversely, 13186-450 hardens more due to β'' precipitation, with some contribution from β' precipitation. Although the overall strength gains due to artificial aging are not significantly different for the two samples (Table II), the presence of proportionately more of the relatively coarse, semi-coherent β' in 13185-450-170 may be responsible for degrading its K_{eq} more. In general, therefore, it is desirable to obtain hardening during aging mainly from coherent precipitates, which do not serve as void nucleation sites.

13185-450 vs. 13186-450 Thermogram

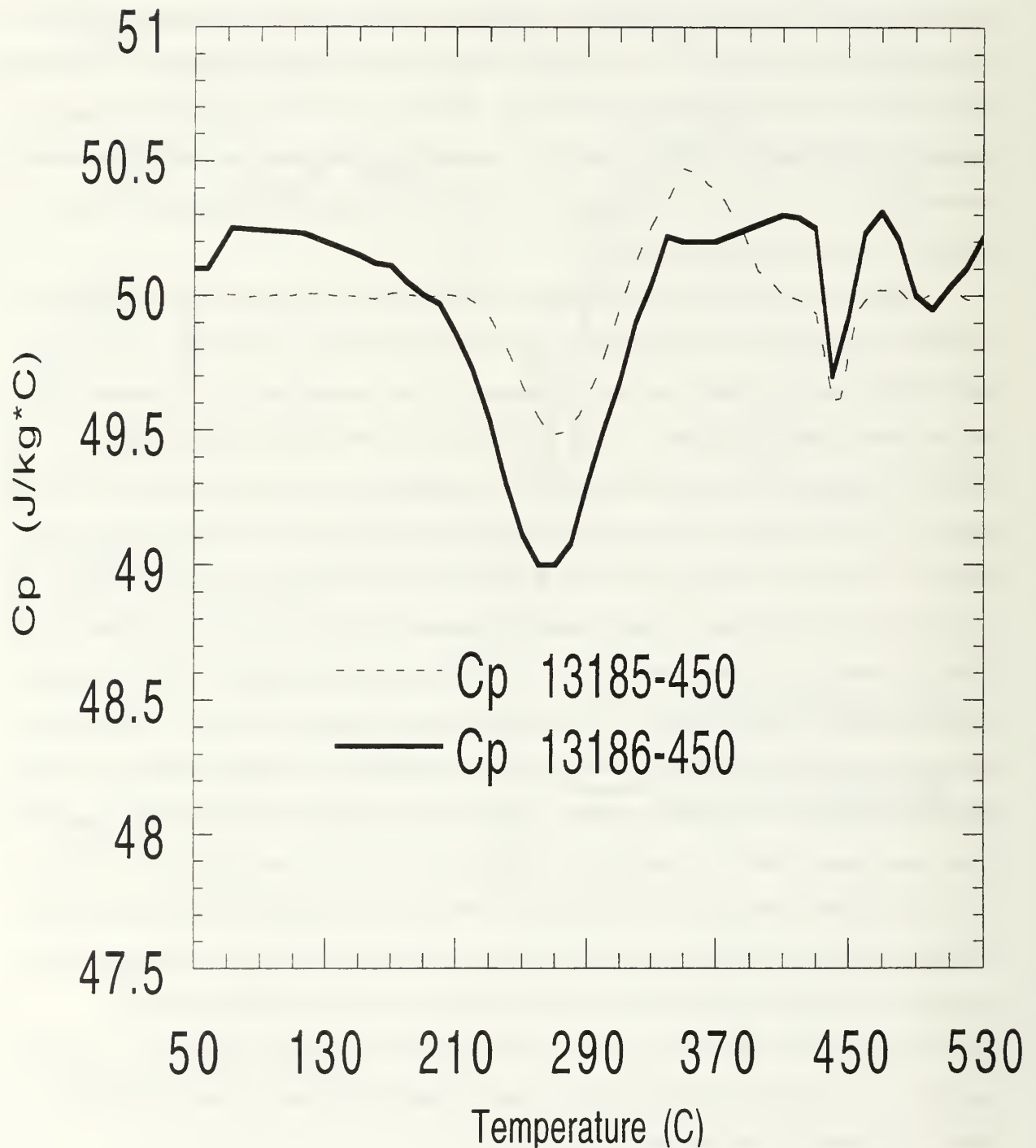


Figure 40: DSC Thermogram for 13185-450 and 13186-450.

Figure 41 shows DSC thermograms of the 13185 sample following full solutionization at 560°C and a solution anneal at 450°C (13185-560 and 13185-450). Overall, the same behavior as that of 13186 (Figure 38) is observed, although the amounts of the precipitates obtained are different. Thus, deformation processing history (particularly, extrusion temperature and strain rate) may influence the details of the precipitation behavior, although the overall precipitation processes remain the same.

Figure 42 shows DSC thermograms of 13185-450 and 13185-560-450. The first sample represents the condition following a 450°C solution anneal, whereas the second represents a full solutionization at 560°C followed by a solution anneal at 450°C. It is apparent that in the -560-450 condition, less solute is available for precipitation than from the -450 condition. This suggests that more hardening precipitates are present in 13185-560-450 than in 13185-450, in agreement with Table II, which shows that the yield strength of 13185-560-450 is greater than that of 13185-450 (225 vs 160 MPa). During the 450°C solution anneal immediately after the extrusion at 400°C the incoherent precipitates already present would be expected to undergo some Ostwald ripening, with some additional incoherent β precipitates forming. During the 450°C solution anneal after a 560°C solutionization, on the other hand, precipitation starts anew directly from the solid solution. Since the quenched-in vacancy concentration in this condition is much greater, any transition precipitate with a solvus temperature above 450°C can nucleate easily, with additional nucleation occurring at the matrix dislocations, which are expected to be more prolific in this condition because of the higher temperature of solution treatment. These transition precipitates age rapidly into semi and incoherent precipitates, thus putting the matrix in a more advanced state of aging than in the 450°C solution annealed condition, where precipitation sites are comparatively scarce. Consequently, as observed from Table II, during subsequent artificial aging at 170°C less yield strength gain is achieved for 13185-560-450 (225 to 310 MPa) than for 13185-450 (160 to 270 MPa). Despite this significantly enhanced yield strength level, K_{eq} of the 13185-560-450-170 is only slightly lower than that of 13185-450-170 (29.7 vs 31.2 MPa), possibly because of the finer dispersion of precipitates in the former.

Figure 43 shows DSC thermograms of the 13186 sample after solution anneals at 450°C and 480°C (13186-450 and 13186-480). At the higher temperature, more of the incoherent

13185-560 vs. 13185-450

Thermogram

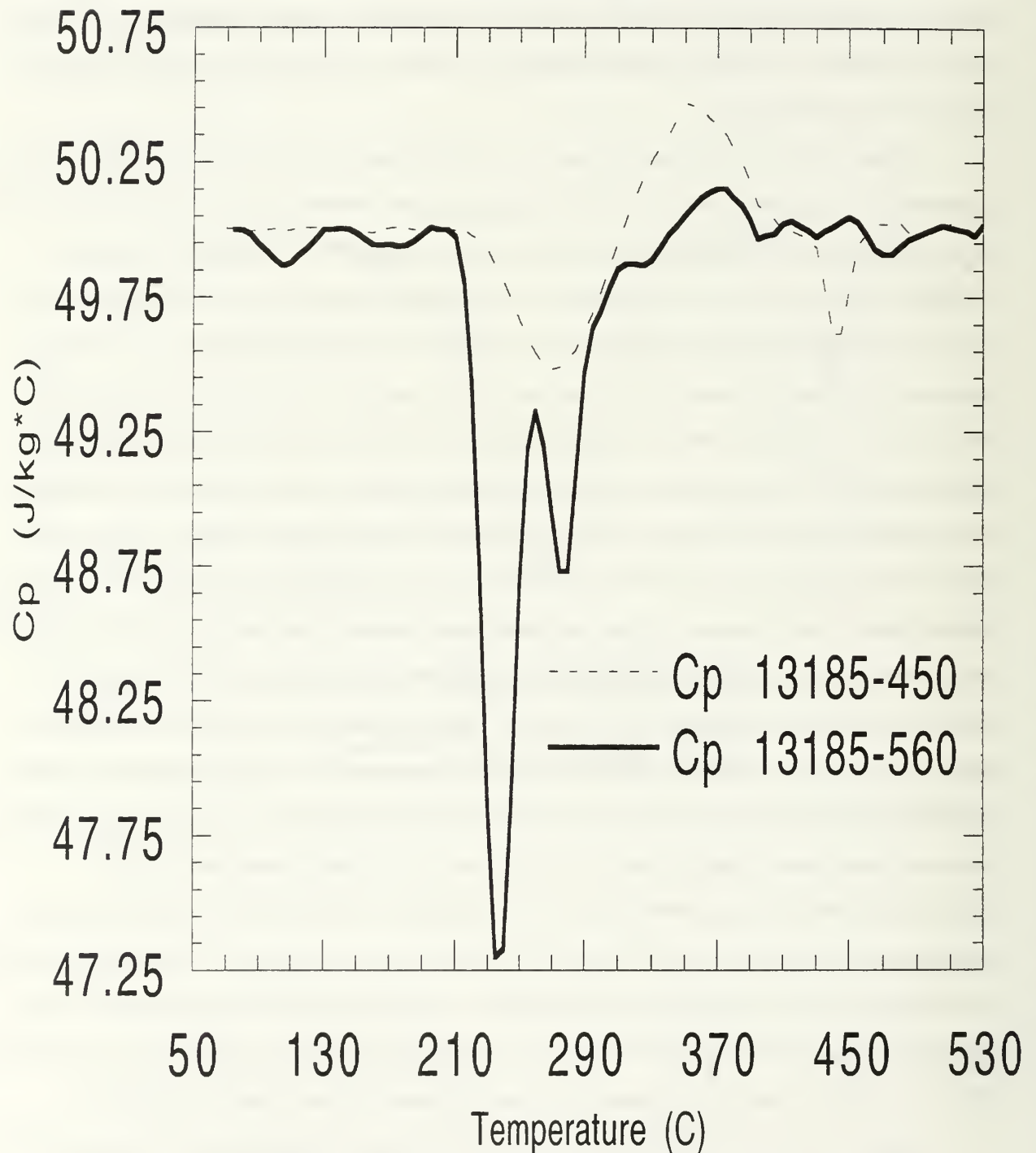


Figure 41: DSC Thermogram for 13185-560 and 13185-450.

13185-450 vs. 13185-560-450 Thermogram

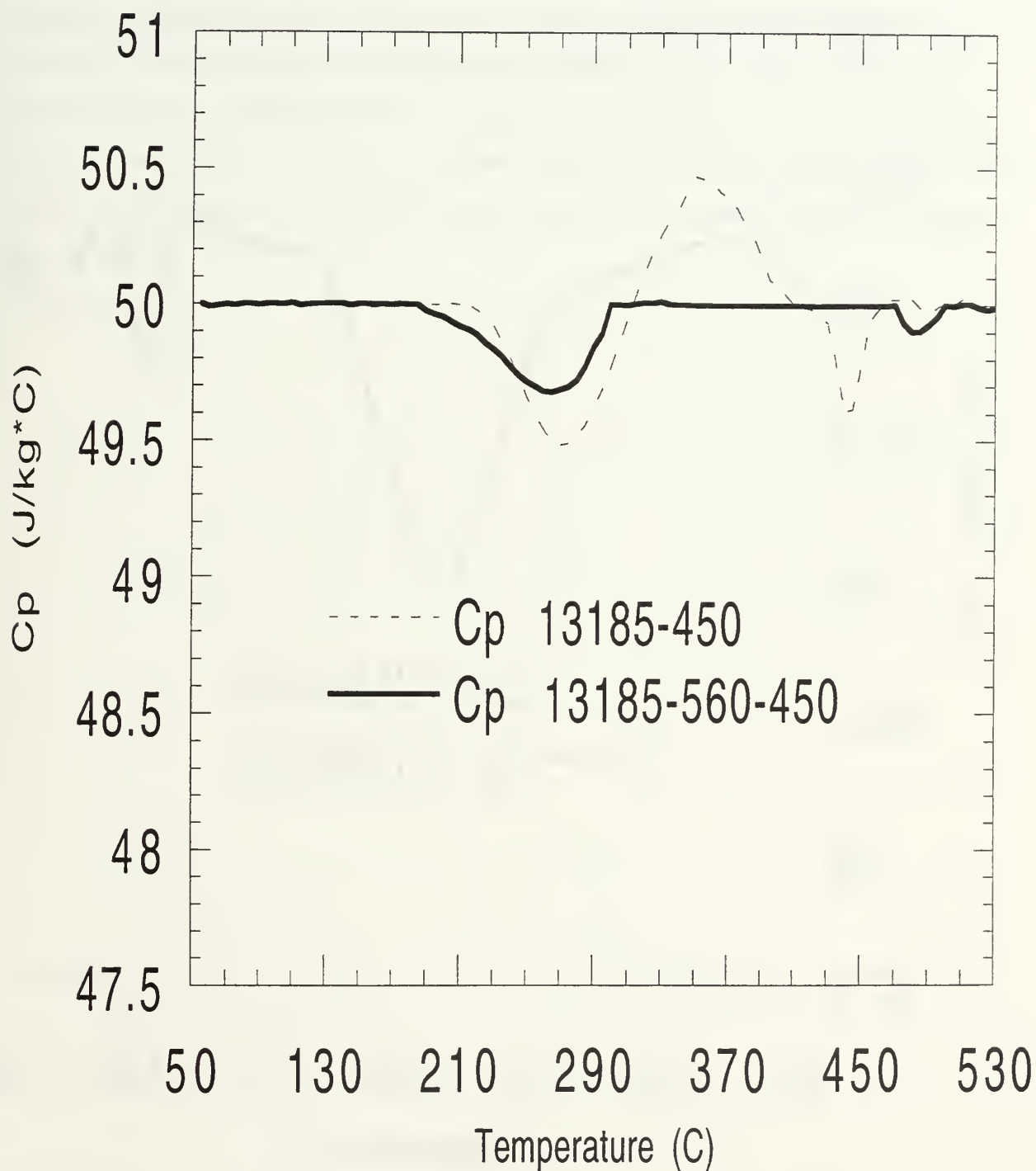


Figure 42: DSC Thermogram for 13185-450 and 13185-560-450.

13186-480 vs. 13186-450

Thermogram

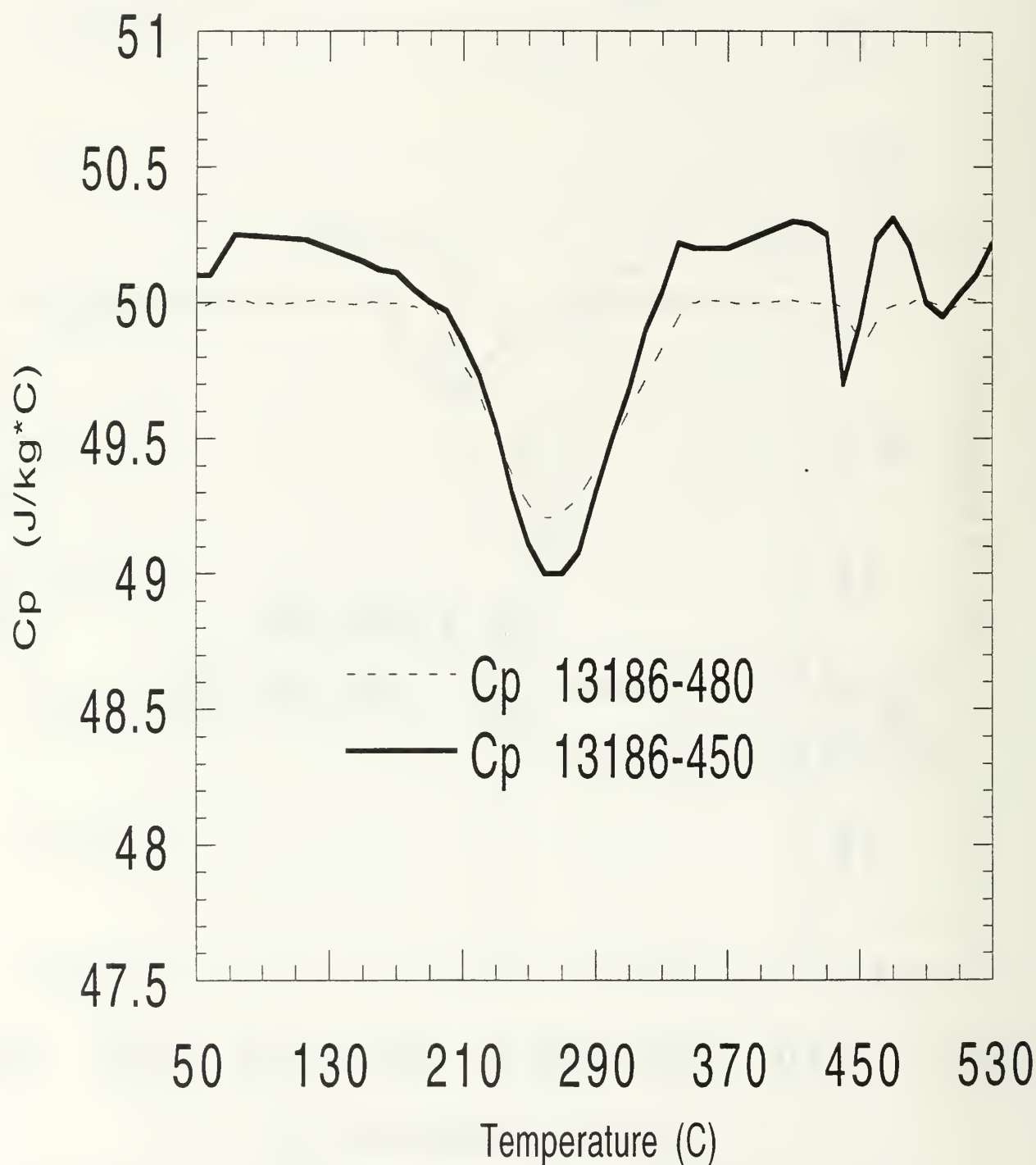


Figure 43: DSC Thermogram for 13186-480 and 13186-450.

precipitates form and grow coarser, leaving less for subsequent precipitation. Because of this rapid coarsening of the β precipitates during the solution anneal, the -480-170 sample consistently demonstrates a lower fracture toughness than the -450-170 sample, attributable, in addition to its somewhat higher strength level, to the ease of void nucleation at coarse, incoherent precipitates. Thus, it is clear that any solution anneal treatment directly after the extrusion process should be conducted at as low a temperature as practicable (i.e., at or around the prior extrusion temperature, provided this is adequate to cause recrystallization), so that as much of the solute as possible can be left in solution to provide additional hardening following subsequent artificial aging.

V. SUMMARY

In summary, based on the above mechanical testing and calorimetric studies, it is apparent that the heat treatment conditions which produced desirable strength-toughness combinations spanning over a wide range are :

- | | |
|----------------------|---|
| 1. 13185-T6 | ($\sigma_{YS} = 455 \text{ MPa}$, $K_{Ic} = 27 \text{ MPa-m}^{1/2}$) |
| 2. 13185-T4 | ($\sigma_{YS} = 345 \text{ MPa}$, $K_{Ic} = 28 \text{ MPa-m}^{1/2}$) |
| 3. 13185-560-450-170 | ($\sigma_{YS} = 310 \text{ MPa}$, $K_{Ic} = 30 \text{ MPa-m}^{1/2}$) |
| 4. 13185-560-450 | ($\sigma_{YS} = 225 \text{ MPa}$, $K_{Ic} = 32 \text{ MPa-m}^{1/2}$) |
| 5. 13185-450 | ($\sigma_{YS} = 160 \text{ MPa}$, $K_{Ic} = 39 \text{ MPa-m}^{1/2}$) |

Of the above, the first three are within the yield strength range to produce an advantage over monolithic 6061 Al, and only number 3 has the potential of offering both yield strength and toughness advantages over monolithic 6061 ($\sigma_{YS} = 276 \text{ MPa}$, $K_{Ic} = 29 \text{ MP-m}^{1/2}$), while producing a 48.5% stiffness advantage ($E_{comp} = 104 \text{ GPa}$ vs $E_{mono} = 70 \text{ GPa}$) . However, since the tested sample of 13185-560-450-170 did not satisfy plane strain conditions, further tests need to be conducted to determine its toughness level accurately.

Of the various heat treatments, the 480°C solution anneal was found not to produce desirable results, and produced properties consistently worse than the other heat treatments in all extrusion conditions.

Further, of the various extrusion conditions examined, the best as noted earlier, the best properties were obtained from the process condition corresponding to Particle Stimulated Nucleation (PSN) of recrystallization, although this advantage is minimal in the intermediate strength-toughness range.

VI. CONCLUSIONS

Based on the above, the following conclusions can be drawn:

1. Secondary processes which produce homogeneous particulate distributions within the DRA matrix, and yield microstructures containing fine matrix grains and a suitable distribution of hardening precipitates, have the potential of offering better fracture toughnesses-strength combinations than monolithic Al alloys.
2. In order to obtain high fracture toughnesses, an intrinsically tough matrix which is hard enough to permit loading of SiCp, but soft enough to preclude their premature failure is desirable, so that eventual fracture progresses through the matrix in the absence of particle cracking.
3. Complete PSN of recrystallization, resulting in a fine matrix grain size with highly misoriented grain boundaries, yields the best properties, with the advantage over the non-PSN state being more pronounced at the low and high strength levels, but less so in the intermediate strength range.
4. In order to achieve high fracture toughness, a refined matrix grain size via PSN, uniform reinforcement distribution, incoherent/semi-coherent/coherent hardening precipitates, and high angle grain boundaries are necessary.
5. PSN provides a considerable increase in K_{eq} , with a relatively smaller increase in tensile ductility.

LIST OF REFERENCES

1. McNelley, T.R., Kalu, P.N., "The Effects of Thermomechanical Processing on the Ambient Temperature Properties and Aging Response of a 6061 Al-Al₂O₃ Composite," *Scripta METALLURGICA et MATERIALIA*, Vol. 25, pp. 1041-1046, 1991.
2. Humphreys, F.J., "The Nucleation of Recrystallization at Second Phase Particles in Deformed Aluminum," *Acta Metallurgica*, Vol. 25, pp. 1323-1344, 1977.
3. Humphreys, F.J., Miller, W.S., Djazeb, M.R., "Microstructural Development During Thermomechanical Processing of Particulate Metal-Matrix Composites," *Materials Science and Technology*, Vol. 6, pp. 1157-1166, 1990.
4. Kalu, P.N., McNelley, T.R., "Microstructural Refinement by Thermomechanical Treatment of a Cast and Extruded 6061 Al-Al₂O₃ Composite," *Scripta METALLURGICA et MATERIALIA*, Vol. 25, pp. 853-858, 1991.
5. Xia, X., Sakaris, P., McQueen, H.J., "Hot Deformation, Dynamic Recovery, and Recrystallisation Behaviour of Aluminum 6061-SiCp Composite," *Material Science and Technology*, Vol. 10, pp. 487-496, 1994.
6. Dutta, I., Allen, S.M., "A Calorimetric Study of Precipitation in Commercial Aluminum Alloy 6061," *Journal of Material Science Letters*, Vol. 10, pp.323-326, 1991.
7. Dutta, I., Allen, S.M., Hafley, J.L., "Effect of Reinforcement on the Aging Response of Cast 6061 Al-Al₂O₃ Particulate Composites," *Metallurgical Transactions A*, Vol 22A, pp. 2553-2563, 1991.
8. Nieh, T.G., Karlak, R.F., *Scripta Metall.*, Vol 18, p. 25, 1984.
9. Dutta, I., Bourell, D.L., *Mater. Sci. Eng.*, Vol. A112, p. 67, 1989.
10. Christman, T., Suresh, S., *Acta Metall.*, Vol. 36, p. 1691, 1988.
11. Papazian, J.M., *Metall. Trans. A*, Vol. 19A, pp. 2945-2953, 1988.
12. Dutta, I., Bourell, D.L., *Acta Metall.*, Vol. 38, p. 2041, 1990.
13. Hunt, W.H. Jr., Osman, T.M., Lewandowski, J.J., "Micro- and Macrostructural Factors in DRA Fracture Resistance," *Journal of Materials*, Vol. 45, No.1, pp. 30-35, Jan 1993.

14. Lewandowski, J.J., Liu, C., "Effects of Matrix Microstructure and Particle Distribution on Fracture of Aluminum Metal Matrix Composite," *Materials Science and Engineering*, Vol. A107, pp. 241-255, 1989.
15. Manoharan, M., Lewandowski, J.J., "Crack Initiation and Growth Toughness of an Aluminum Metal-Matrix Composite," *Acta Metall. Mater.*, Vol. 38, No. 3, pp. 489-496, 1990.
16. Lloyd, D.J., "Aspects of Fracture in Particulate Reinforced Metal Matrix Composites," *Acta Metall. Mater.*, Vol. 39, No. 1, pp. 59-71, 1991.
17. Wei, R.P., Gangloff, R.P., *Fracture Mechanics Perspectives and Directions Twentieth Symposium ASTM STP 1020*, Argon, A.S., "The Role of Heterogeneities in Fracture," pp. 127-148, ASTM, Philadelphia, PA, 1987.
18. Mortenson, A., *Fabrication of Particulates Reinforced Metal Composites*, ASM, Materials Park, OH, p. 217, 1990.
19. Lewandowski, J.J., Liu, D.S., Liu, C., "Observations on the Effects of Particulate Size and Superposed Pressure on Deformation of Metal Matrix Composites," *Scripta METALLURGICA et MATERIALIA*, Vol. 25, pp. 21-26, 1991.
20. Hunt, W.H., Jr., Brockenbrough, J.R., Magnusen, P.E., "An Al-Si-Mg Composite Model System: Microstructural Effects on Deformation and Damage Evolution," *Scripta METALLURGICA et MATERIALIA*, Vol. 25, pp. 15-20, 1991.
21. Dutta, I., Majumdar, M.S., "Effect of Processing on the Fracture Characteristics of a 6092 Al Composite Reinforced with SiCp," to appear in Proc. 5th International Conference on Aluminum Alloys, Grenoble, France, 1-5 July 1996.
22. Argon, A.S., Im, J., Safoglu, R., "Cavity Formation from Inclusions in Ductile Fracture," *Metallurgical Transactions A*, Vol. 6A, pp. 825-837, 1975.
23. Nageswara Rao, B., Acharya, A.R., "Evaluation of J_c from the Recorded Front Face Displacement on CT Specimens," *Engineering Fracture Mechanics*, Vol. 24, No. 4, pp. 625-628, 1986.
24. Nageswara Rao, B., Acharya, A.R., "Evaluation of Fracture Toughness Through J_{Ic} Testing with Standard Compact Tension Specimen," *Experimental Techniques*, Vol. 16, pp. 37-39, Jan/Feb 1992.
25. Orange, T.W., "Crack Displacements for J_I Testing with Compact Specimens," *International Journal of Fracture*, Vol. 19, pp. R59-R61, 1982.

26. Xiao Guang Ning., Zu Han Lai, "Realization of Single Specimen Analytical Method of JIc Determination by Using Compact Tension Loading," *Engineering Fracture Mechanics*, Vol. 34, pp. 1013-1021, 1989.
27. Fisher, D.M., Buzzard, R.J., "Experimental Compliance Calibration of the Compact Fracture Toughness Specimen," *NASA TM-81665*, 1980.
28. Shih, C.F., German, M.D., Kumar, V., "An Engineering Approach for Examining Crack Growth and Stability in Flawed Structures," *Int. J. Pre. Ves. & Piping*, Vol. 9, pp. 159-196, 1981.
29. Tada, H., Paris, P.C., Irwin, G.R., *The Stress Analysis of Cracks Handbook*, Del Research Corporation, 1973.
30. Roberts, E. Jr., "Elastic Crack-Edge Displacements for the Compact Tension Specimen," *Materials Research and Standards*, Vol. 9, No. 2, p. 27, 1969.
31. Dutta, I., " An Investigation of the Effect of Post-Fabrication Processing on the Microstructure and Properties of a SiCp - 6092 Al Composite," Air Force Office of Scientific Research, Bolling AFB, Washington D.C. and Wright Laboratory (MLLM) WPAFB, Dayton, OH, August 1995.

INITIAL DISTRIBUTION LIST

1. Defense Technical Information Center.....2
8725 John J. Kingman Rd., STE 0944
Ft. Belvoir, Virginia 22060-6218

2. Dudley Knox Library.....2
Naval Postgraduate School
411 Dyer Rd.
Monterey, California 93943-5101

3. Naval Engineering, Code 34.....1
Naval Postgraduate School
Monterey, California 93943-5100

4. Department Chairman, Code ME/Mc.....1
Department of Mechanical Engineering
Naval Postgraduate School
Monterey, California 93943-5000

5. Professor I. Dutta, Code ME/Du.....1
Department of Mechanical Engineering
Naval Postgraduate School
Monterey, California 93943-5000

6. Dr. Wilbur Simmons.....1
Material Science Division
U.S. Army Research Office
P.O. box 12211
Research Triangle Park
North Carolina, 27709-2211

7. Dr. Joe Wells.....1
Army Research Lab
AMRSL-MA-CA
APG, Maryland, 21005-5069

8. Dr. Ernest Chin.....1
Army Research Lab
AMRSL-MA-MR
APG, Maryland, 21005-5069

9. Dr. Dan Miracle.....1
Wright Laboratory
WL/MLLM
WPAFB, Ohio, 45433

10. Dr. B.S. Majumdar.....1
Wright Laboratory
WL/MLLM
WPAFB, Ohio, 45433

11. Dr. Benji Maruyama.....1
Wright Laboratory
WL/MLLM
WPAFB, Ohio, 45433

12. Dr. M.L. Gambone.....1
Wright Laboratory
WL/MLLM
WPAFB, Ohio, 45433

13. Dr. Steve Fishman.....1
Office of Naval Research
800 N. Quincy St.
Arlington, Virginia, 22217-5000

14. Mr. Ted Muha.....1
MMCIAC
CINDAS/Purdue University
1293 Potter Engineering Center, Room 376
West Lafayette, Indiana, 47907-1293

15. Dr. Don Lesver.....1
Lawrence Livermore National Laboratory
P.O. Box 808
Livermore, California, 94550

16. Prof. M. Rosen.....1
102 Maryland Hall
3400 N. Charles St.
Baltimore, Maryland, 21218-2689

17. Prof. J. Spicer.....1
102 Maryland Hall
3400 N. Charles St.
Baltimore, Maryland, 21218-2689
18. Mr. Mark van den Bergh.....1
DWA Composite Specialties
21130 Superior St.
Chatsworth, California, 91311-4393
19. LT Frank N. Quiles, USN.....2
1556 Union Blvd.
Bay Shore, New York, 11706

DUDLEY KNOX LIBRARY
NAVAL POSTGRADUATE SCHOOL
MONTEREY CA 93943-5101

DUDLEY KNOX LIBRARY



3 2768 00323846 0